nature portfolio

Peer Review File

Bipolar membranes reveal surface-hydroxyl-structure-dependent water dissociation mechanism

Corresponding Author: Professor Yuhang Wang

This file contains all reviewer reports in order by version, followed by all author rebuttals in order by version.

Version 0:

Reviewer comments:

Reviewer #1

(Remarks to the Author)
This manuscript reports the design of SnO2 quantum wires (QWs) for bipolar membrane water dissociation (WD) catalyst and investigates the specific role of hydroxyl groups in enhancing the WD kinetics. The central hypothesis that engineered surface hydroxyls adsorbed on the bridging oxygen vacancies (–ObrH) act as pivotal catalytic sites for accelerating the H^+/OH^- generation rate, addressing a critical limitation of BPM performance. The work appears to combine material synthesis, electrochemical characterization, and theoretical calculations, aiming for a mechanistic understanding. While the premise is strong and potentially significant, the manuscript in its current form requires substantial revision to meet the high standards of this journal. The major concerns revolve around the clarity of the proposed mechanism and the overall presentation of data and analysis.
1. The current manuscript lacks sufficient presentation of key information and essential data, such as the fabrication process, characterization, and property studies of the bipolar membranes. Moreover, it provides no information on the anion- and cation-exchange layers, which are essential components of bipolar membranes.
2. The manuscript lacks control experiments (e.g., using conventional SnO2 nanoparticles as water dissociation catalysts), making it impossible to evaluate the relative performance of conventional SnO2 nanoparticles versus SnO2 quantum wires.
3. QWs appear to be a novel material unexplored in bipolar membranes, yet their rationale for use is not addressed in the manuscript. Why were QWs selected, and what advantages do they offer over commercial, readily synthesized conventional nanoparticles?
4. The authors propose two water dissociation mechanisms under acidic and alkaline environments. Is this hypothesis supported by solid theoretical or experimental evidence? Given that both protons and hydroxide ions are simultaneously generated during water dissociation reaction, which pathway predominates under each condition?
5. On page 8 of the manuscript, the authors state that “Together with the EPR results, we concluded that both i-Ov and b-Ov concentrations increase with longer synthesis durations” which appears to contradict the data in Supplementary Table 4, where the concentration of i-Ov decreases over reaction time. Furthermore, the characterization and quantitative analysis presented here appear to constitute critical experimental evidence, yet the manuscript lacks sufficient interpretation, making it difficult for readers to understand how the surface oxygen species are quantified.
6. Regarding central conclusion that –ObrH govern the kinetics of water dissociation on SnO2, the argument relies heavily on molecular simulations and lacks direct experimental evidence, which weakens its persuasiveness.
7. For mechanistic studies of water dissociation catalysts in bipolar membranes, current densities should generally remain moderate (0–100 mA cm–2), as higher current densities are limited by water supply to the bipolar membrane interior. In this manuscript, however, the electrochemical characterization is performed at relatively high current densities (500 and 1000 mA cm–2), which risks obscuring the genuine reaction and mass transport behavior in the water dissociation regime.

Reviewer #2

(Remarks to the Author)
This manuscript offers an insightful look into how the enrichment of bridging hydroxyl species (–ObrH) boosts the alkaline water dissociation (WD) process on SnO2 quantum wires. By combining thoughtful theoretical analysis with solid experimental evidence, it clearly shows that this enhancement is due to specific surface chemistry rather than to surface area alone. Overall, the study is interesting and relevant, providing both fundamental insights and practical performance data. Addressing the points above would enhance clarity and help computationally oriented readers follow the mechanistic

conclusions more easily.

1. The SnO_2(110) surface is a classic example of a rutile-type oxide, widely used in computational research. It would be helpful if the authors could include a brief explanation or cite relevant sources for their choice of a Sn-exposed surface rather than an O-terminated one, especially in the context of water dissociation. This discussion would clarify why this termination is particularly useful for highlighting the active bridging hydroxyl sites (–ObrH) and the associated alkaline WD process.

2. The site's pKa is described via the two-state free energy difference. In Figure 3b, the reference state is (0, 0), and the second state is (1.0, 12). A local minimum exists between these points. Could the authors clarify why this intermediate was not used as the final state? A similar issue applies to Figure 3c.

3. The PES is explored using the DPMD method. Given that machine-learned molecular dynamics performed poorly beyond the training data, it would be helpful if the authors could provide additional details on the composition of the training and test datasets. Could the author share more details about the training and test data?

4. DFT calculations were performed using a planewave energy cutoff of 400 Ry with the PBE functional. Please verify that this cutoff is sufficient.

5. The discussion primarily focuses on SnO_2-derived surfaces, raising questions about whether WD promotion is due to a general structure–activity principle linked to bridging hydroxyl motifs on rutile oxides or to a material-specific effect tied to the electronic properties of Sn–O bonding. Clarifying these aspects could strengthen the mechanistic argument and its broader relevance. To assess the transferability of the structure–activity relationship, oxide surfaces with similar bridging oxygen coordination environments could be studied under comparable conditions. Otherwise, the mechanism's consistency across different interfacial pH environments and membrane configurations.

6. While the reported stability metrics are impressive, briefly clarify the structural or chemical persistence of –ObrH under prolonged high-current operation. Including post-operation characterization (e.g., spectroscopic confirmation in the Supplementary Information) or discussing dynamic regeneration of –ObrH sites during operation would strengthen the work.

Reviewer #3

(Remarks to the Author)
The authors present a mechanism-oriented materials study that combines theory-driven design with experimental validation to elucidate structure–reactivity relationships in water dissociation within bipolar membranes. The work reveals the role of surface hydroxyl coordination in determining the reaction pathway and kinetics of water dissociation. This is imperative for understanding this fundamental process and developing more efficient catalysts and bipolar membranes. Overall, the study is timely and important. Several aspects of the manuscript require improvement. Issues in interpreting observed correlations, in data presentation, in performance comparisons with competing electrolyzer configurations, and in degradation mechanisms must be addressed. I therefore recommend major revision, with the expectation that a carefully revised manuscript addressing the points raised below would be suitable for publication.

1.Line 107: The statement "These Ovs would transform into surface hydroxyls via water adsorption and dissociation" lacks sufficient supporting evidence. The authors are encouraged to validate this claim with either experimental or computational evidence.

2.What would happen if the synthesis duration of SnO_2 QWs is extended beyond 10 h? Will the ratios between different hydroxyls change, and will the observed correlation stay monotonic?

3.What are the meanings of the numbers in Fig. 4c, and how did the authors obtain them? Clarification and calculation details are apparently required to support the argument that "These results collectively demonstrate the link between TMV reduction and surface –ObrH (Fig. 4c). In contrast, other reported activity descriptors, including surface areas, particle diameters, and electrical conductivity (Supplementary Table 5), show irrelevance to the observed WD activity improvement."

4.More broadly, while the use of acidic HER and alkaline OER in a reverse-bias BPM electrolyzer is mechanistically appealing, the voltage penalty associated with water dissociation at the BPM interface (reported as ~0.68 V at 100 mA cm^{-2}) appears substantial. From a system-level energy-efficiency perspective, this penalty may outweigh the kinetic benefits of avoiding alkaline HER and acidic OER. In contrast, anion exchange membrane water electrolysis (AEMWE) operates in a similar alkaline OER environment but incurs its primary kinetic penalty only at the HER, without an additional water-dissociation voltage loss.

The authors are therefore encouraged to compare the performance of their BPM water electrolyzer to that of state-of-the-art AEMWEs operated under comparable conditions. This helps clarify how much of the observed performance gap must be bridged for BPMs to become competitive, and under what scenarios—if any—the BPM approach offers a net advantage. Addressing this point would significantly strengthen the manuscript's relevance to the broader water electrolysis community.

5.The attribution of activity degradation to Co_3O_4 dissolution (Line 299) remains speculative, as it relies solely on the qualitative observation of the anolyte turning yellowish. This causal link must be quantitatively substantiated. The authors should:
1)Quantify metal crossover: Utilize ICP-OES/MS to measure the concentration of dissolved Cobalt species in the anolyte at

specific time intervals.
2)Post-mortem analysis on the spent Co3O4 electrode.

6.It might be helpful to check whether the density computed from the MLMD trajectory is reasonable.

7.Fig. 4f appears intended to benchmark the performance of the present system against literature-reported state-of-the-art values. However, such comparisons are not straightforward, as reported performance metrics strongly depend on experimental conditions, including temperature, effective electrode area, electrolyte composition, and cell configuration. I recommend that the authors provide a more detailed summary of the experimental conditions associated with the literature data points, ideally in the Supplementary Information.

Version 1:

Reviewer comments:

Reviewer #1

(Remarks to the Author)
The authors have clarified all concerns in the previous comments letter. The revised version can be accepted for publication.

Reviewer #2

(Remarks to the Author)
The authors have addressed all my comments. I recommend that it can be accepted.

Reviewer #3

(Remarks to the Author)
I have no more concern. A well work.

Response to reviewers
Manuscript NCOMMS-25-98484-T

We sincerely thank the Editor and the Reviewers for their careful evaluation of our manuscript and for the constructive comments that have significantly helped improve the clarity and rigor of this work.

In response to the comments, we have substantially revised the manuscript and Supplementary Information. The major revisions include additional control experiments, expanded structural and electrochemical characterization, quantitative degradation analysis, and clarification of the mechanistic interpretation. All changes have been clearly indicated in the revised manuscript and are summarized below.

Below, we provide a detailed point-by-point response to each comment.

Reviewer 1: pages 2-19
Reviewer 2: pages 20-26
Reviewer 3: pages 27-41

For Reviewer #1

This manuscript reports the design of SnO_2 quantum wires (QWs) for bipolar membrane water dissociation (WD) catalyst and investigates the specific role of hydroxyl groups in enhancing the WD kinetics. The central hypothesis that engineered surface hydroxyls adsorbed on the bridging oxygen vacancies ($-O_{br}H$) act as pivotal catalytic sites for accelerating the H^+/OH^- generation rate, addressing a critical limitation of BPM performance. The work appears to combine material synthesis, electrochemical characterization, and theoretical calculations, aiming for a mechanistic understanding. While the premise is strong and potentially significant, the manuscript in its current form requires substantial revision to meet the high standards of this journal. The major concerns revolve around the clarity of the proposed mechanism and the overall presentation of data and analysis.

Reply:

We thank the reviewer for recognizing the novelty and significance of our work and for raising the following important points that will help us improve our manuscript. In light of the reviewer's invaluable suggestions and comments, we have conducted new experiments and made clarifications/revisions to our manuscript.

Comment 1

The current manuscript lacks sufficient presentation of key information and essential data, such as the fabrication process, characterization, and property studies of the bipolar membranes. Moreover, it provides no information on the anion- and cation-exchange layers, which are essential components of bipolar membranes.

Reply:

In response to this comment, we have added a schematic illustration of the BPM fabrication procedure (**Figure R1**) that clearly shows the sequential deposition of the ionomer and catalyst interlayers, as well as the hydration step.

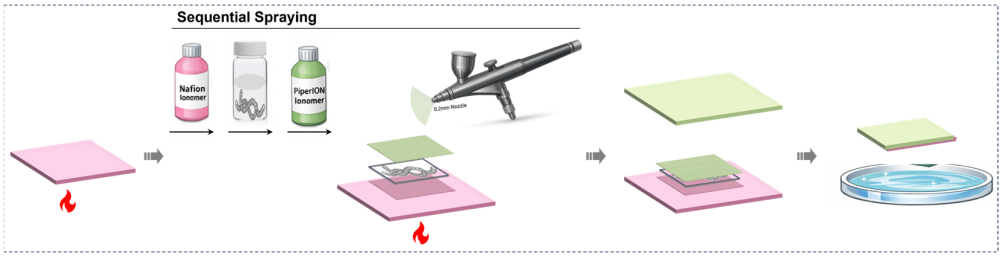

Figure R1. Schematic illustration of the fabrication process for BPMs.

We have also included additional structural and electrochemical characterization of the BPM, including SEM images of the catalyst-coated membrane (**Figure R2**) and low-current-density polarization measurements (**Figure R3**) to assess the first limiting current density and the intrinsic water dissociation behavior in the kinetic-controlled regime.

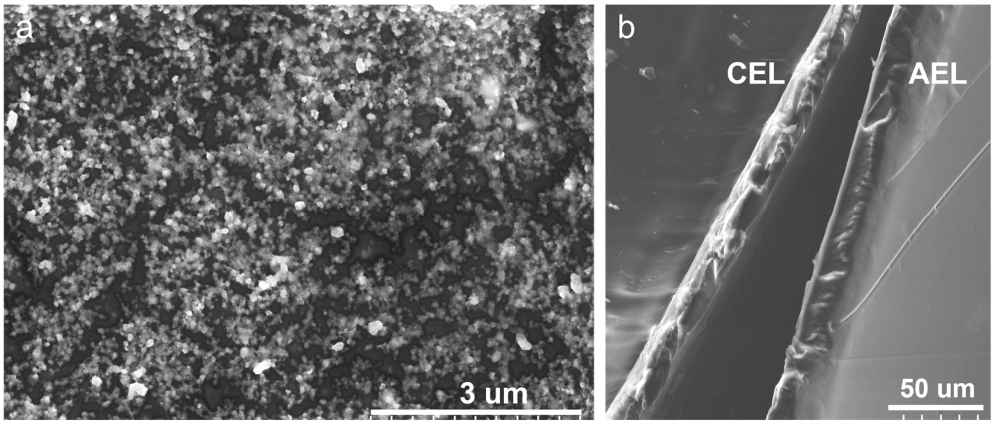

Figure R2. Morphology characterization of the BPM. SEM images of QWs10 on the CEL (a) and BPM cross-section (b).

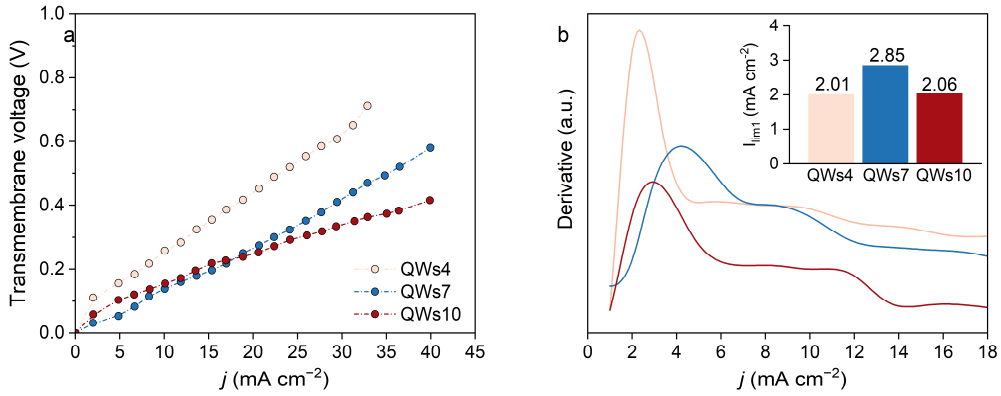

Figure R3. Water dissociation performance of the QWs in the kinetic-controlled regime. (a) j-V (0 ~ 50 mA cm^{-2}) and (b) corresponding derivative curves (dV/dj). Source data are provided as a Source Data file.

The extracted first limiting current densities are ~2.0, 2.9, and 2.1 mA cm^{-2} for QWs4, QWs7, and QWs10, respectively, suggesting broadly similar bulk membrane transport properties (e.g., thickness, ion-exchange capacity, and intrinsic ionic conductivity) under the tested conditions. Accordingly, the variations in WD activity are primarily attributed to differences in interfacial catalytic properties, consistent with the structure–activity relationship discussed in this work.

In addition, to address the lack of information regarding the exchange layers, we have added a summary table (**Table R1**) reporting the key physical and electrochemical properties of the membranes used in this study, namely Nafion NR211 (CEL) and PiperION-A20-HCO_3 (AEL). The reported parameters include thickness, mechanical strength, ion-exchange capacity (IEC), ionic conductivity, water uptake, and swelling ratio, as provided by the suppliers.

Table R1. The information on the anion- and cation-exchange layers.

Membrane	Thickness (μm)	Ultimate Tensile Strength-Max (MPa)	IEC (H^+ or OH^-)	Conductivity (mS cm^{-1}, 80 °C)	Water Uptake (%)	Swelling Ratio (%)
Nafion NR211 (CEL)	25	23 (MD) 28 (TD)	0.92 (H^+, meq/g)	100 (100% RH)	5.0±3.0%	50±5%
PiperION-A20-HCO_3 (AEL)	20	> 30	2.35 (OH^-, meq/g)	150 (OH^-)	8.0±3.0%	50 (80 ℃ in 1M KOH)

We added **Table R1** as **Supplementary Table 7, Figure R1, R3** as **Supplementary Figure 43, 44** to the revised supplementary information.

The following text has been updated in the manuscript:

(Page 20, Lines 405-406) "The key physical and electrochemical properties of these membranes are summarized in Supplementary Table 7."

(Page 21, Lines 421-422) "The fabrication process for BPMs is shown in Supplementary Fig. 43."

(Page 22, Lines 437-442) "The extracted first limiting current densities are ~2.0, 2.9, and 2.1 mA cm^{-2} for QWs4, QWs7, and QWs10 (Supplementary Fig. 44), respectively, suggesting broadly similar bulk membrane transport properties (e.g., thickness, ion-exchange capacity, and intrinsic ionic conductivity) under the tested conditions. Accordingly, the variations in WD activity are primarily attributed to differences in interfacial catalytic properties, consistent with the structure–activity relationship discussed in this work."

Comment 2

The manuscript lacks control experiments (e.g., using conventional SnO_2 nanoparticles as water dissociation catalysts), making it impossible to evaluate the relative performance of conventional SnO_2 nanoparticles versus SnO_2 quantum wires.

Reply:

We appreciate the reviewer's insightful suggestion. Accordingly, we synthesized SnO_2 quantum dots (QDs) as a control sample and evaluated their structural, physical, and electrochemical properties under identical BPM fabrication and testing conditions.

Synthesis of SnO_2 QD catalysts

SnO_2 QDs were also synthesized using a method similar to that for SnO_2 QWs, except that ethanol was replaced with methanol and the reaction time was extended to 18 h. The products were separated by centrifugation at 9000 rpm for 10 min after the addition of 50 mL of ethanol.

The products were washed several times by redispersing in cyclohexane, adding ethanol, and centrifuging. The obtained SnO_2 QDs were further characterized using XRD, TEM, XPS, Raman spectroscopy, and pure water electrolysis to confirm the crystallinity, average size, oxygen deficiency, and WD activity (**Figures R4-9**).

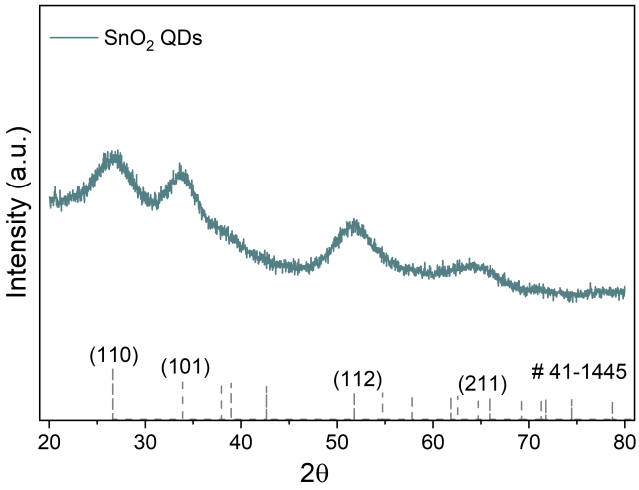

Figure R4. XRD patterns of SnO_2 QDs.

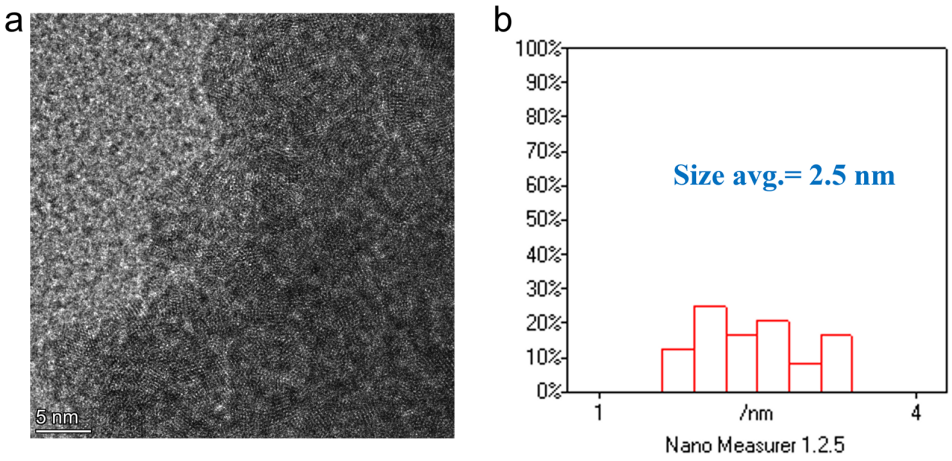

Figure R5. High-resolution transmission electron microscopy (HRTEM) images (a) and corresponding particle size distribution histograms (b) of SnO_2 QDs.

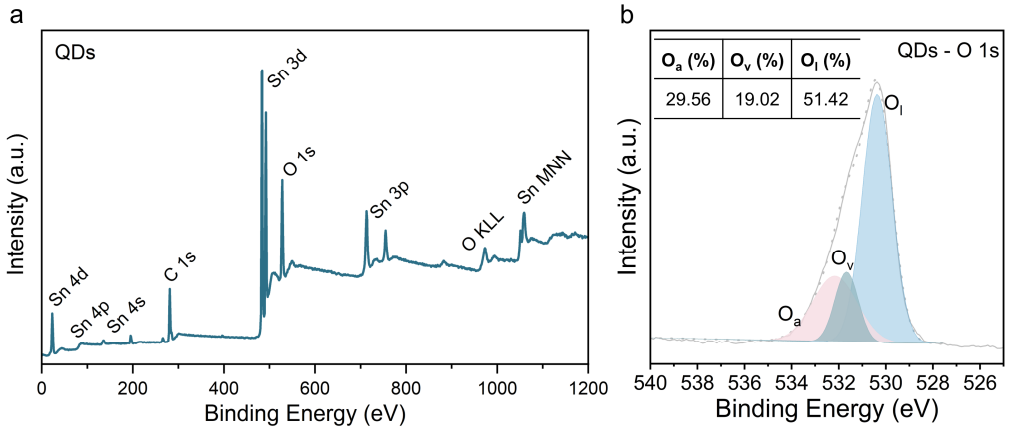

Figure R6. XPS analysis of SnO_2 QDs.

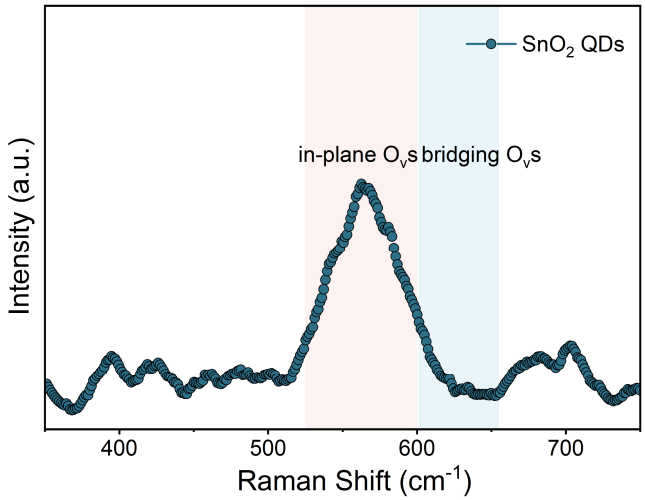

Figure R7. The Raman spectrum of SnO_2 QDs.

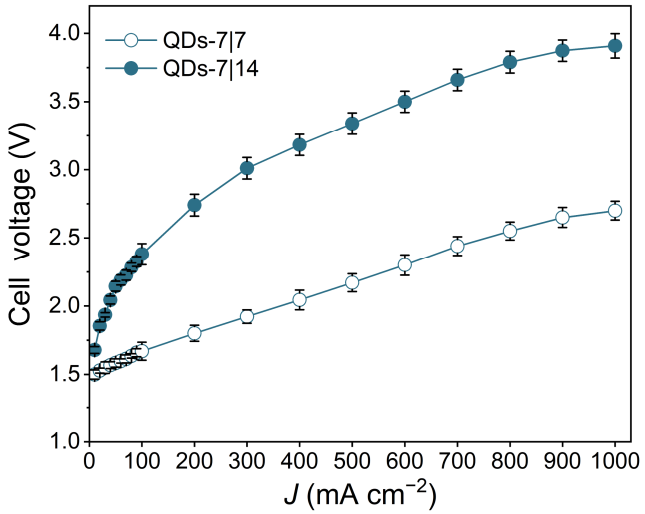

Figure R8. Full cell polarization curves of SnO_2 QDs at a catalyst loading of 14 ug cm^{-2} under different pH gradient conditions: (7|7) and (7|14) at 60 °C.

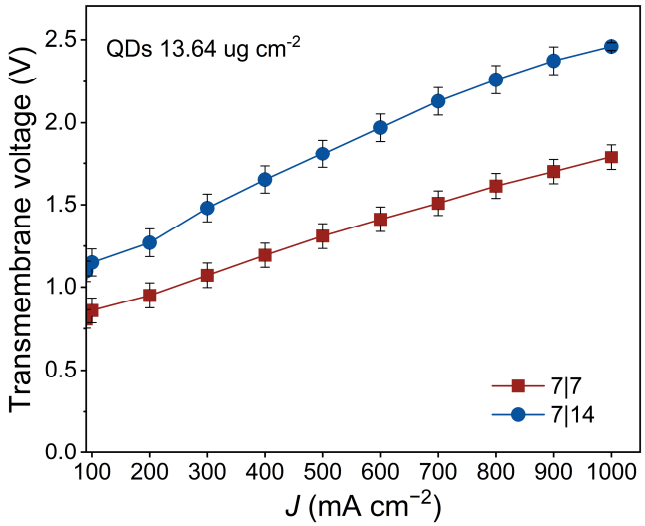

Figure R9. TMVs at different current densities for BPM electrolyzers employing QDs as the water dissociation (WD) catalyst at loadings of 14 μg cm^{-2}, under distinct pH conditions: (7|7), and (7|14) at 60 °C.

The physical parameters of the SnO_2 QDs are summarized in **Table R2**.

Table R2. Physical properties, transmembrane voltage (TMV), and cell voltage (at loading of 14 ug cm^{-2}) of SnO_2 QDs.

Sample	O_v ($\times 10^{12}$ spins g^{-1})	-O_{br}H/b-O_V (%)	TMV (V)	Cell voltage (V)	Surface area (m^2 g^{-1})	Conductivity (S m^{-1})	Diameters (nm)
QDs	5.64	9	1.79	2.70	193	0.0025	2.50

The QDs exhibit an average particle diameter of 2.50 nm and a relatively high specific surface area of 193 m^2 g^{-1}, which is higher than that of the QWs samples. The bulk electrical conductivity (0.00247 S m^{-1}) is comparable to that of the QWs series.

However, oxygen deficiency analysis reveals markedly different surface chemistry. The total oxygen vacancy (O_V) fraction of the QDs is 19%, and the fraction of bridging-vacancy-associated motifs (−O_{br}H/b-Ov) is merely 9%, which is only ~27%, ~21%, ~17%, and ~18% of those in QWs4 (34%), QWs7 (45%), QWs10 (55%), and QWs12 (53%), respectively. Correspondingly, the QDs-based BPM exhibits a higher transmembrane voltage (TMV) of 1.79 V and a cell voltage of 2.70 V at a loading of 14 μg cm^{-2} under the same operating conditions.

This comparison indicates that specific surface area and bulk conductivity do not show a consistent correlation with WD performance in our system. Despite possessing a higher BET surface area and similar conductivity, the QDs show inferior WD activity relative to QWs10. In contrast, the samples with higher −O_{br}H fractions consistently exhibit lower TMV values.

These control experiments therefore support the conclusion that the enhancement in WD kinetics observed for QWs is associated with the enrichment of bridging-vacancy-derived hydroxyl motifs, rather than with geometric surface area or bulk electronic conductivity effects.

We added **Figures R4-R9** as **Supplementary Figure 35,** and the data originally summarized in **Table R2** have been incorporated into **Supplementary Table 5** in the revised supplementary information.

Comment 3

QWs appear to be a novel material unexplored in bipolar membranes, yet their rationale for use is not addressed in the manuscript. Why were QWs selected, and what advantages do they offer over commercial, readily synthesized conventional nanoparticles?

Reply:

We thank the reviewer for appreciating the novelty of our catalyst design. The selection of SnO_2 quantum wires (QWs) is motivated by their ability to establish a structurally continuous catalytic network that facilitates interfacial proton transfer during water dissociation (WD).

During WD, protons must be generated and transferred across catalyst surfaces over nanometer-length scales (*Nat Energy* **9**, 548–558 (2024); *Nat Chem Eng* **1**, 45–60 (2024)). An interconnected catalyst network provides continuous surface pathways that facilitate proton transfer between adjacent sites. In this context, the continuous surface of QWs supports an extended network of surface hydroxyl groups (−OH), enabling more efficient proton transfer between neighboring hydroxyls.

In contrast, nanoparticle-based interlayers form discontinuous domains that introduce spatial interruptions, which can hinder proton transfer across the interface. Therefore, the high structural continuity of QWs is expected to facilitate proton transfer between surface hydroxyls, providing a physically grounded rationale for their improved WD performance.

The manuscript has been revised to clarify this point:

(Page 4, Lines 82-85) “The one-dimensional morphology of QWs could enable uninterrupted pathways to facilitate proton transfer between adjacent sites and mitigate transport limitations in nanoparticle-based systems, thereby providing a physical basis for enhanced WD kinetics.”

Comment 4

The authors propose two water dissociation mechanisms under acidic and alkaline environments. Is this hypothesis supported by solid theoretical or experimental evidence? Given that both protons and hydroxide ions are simultaneously generated during water dissociation reaction, which pathway predominates under each condition?

Reply:

We thank the reviewer for this important mechanistic question. We emphasize that our interpretation does not imply different overall reaction stoichiometries. In all cases, water dissociation proceeds as:

$$H_2O \rightleftharpoons H^+ + OH^-$$

and both ions are generated simultaneously. The distinction discussed in the manuscript refers to the rate-controlling proton-transfer coordinate under different interfacial microenvironments, rather than different overall reactions.

In bipolar membranes, the cation-exchange layer (CEL) and anion-exchange layer (AEL) inherently create distinct local pH environments at the junction under reverse bias. As a result, the WD process occurs in asymmetric microenvironments, with regions adjacent to the CEL being relatively acidic and those near the AEL relatively alkaline. This spatial pH asymmetry leads to different dominant proton-transfer coordinates on catalyst surfaces, giving rise to what we describe as "acidic" and "alkaline" WD regimes.

This interpretation is consistent with prior studies, particularly the work by Oener et al. (Science 369 (6507), 1099-1103 (2020)), which demonstrated that water dissociation activity correlates strongly with the catalyst's point of zero charge (PZC). In the work, catalysts with higher PZC values generally exhibit superior activity under alkaline interfacial conditions (i.e., near the AEL). In contrast, low-PZC materials tend to be less effective in facilitating WD in alkaline environments. This provides an experimental basis for linking surface charge state to the dominant proton-transfer process.

Our observations align with this framework. As a relatively low-PZC oxide (**Figure R10**), SnO_2 QWs exhibit intrinsically reduced WD activity under alkaline conditions (**Fig. 2)**. However, increasing the fraction of bridging oxygen vacancy–associated hydroxyl species ($-O_{br}H$) leads to a systematic enhancement in WD activity, most pronounced under alkaline gradient conditions. This trend establishes a correlation between WD activity and surface hydroxyl coverage.

Combined with our experimentally determined PZC, pH-dependent TMV measurements, and structure–activity correlations, these results support the conclusion that the "predominant pathway" refers to the rate-limiting proton-transfer step under a given interfacial charge state. Specifically, under alkaline conditions (pH > PZC), proton transfer involving deprotonated surface sites becomes more relevant, whereas under acidic conditions (pH < PZC), the process is associated with protonated surface species and hydroxide separation.

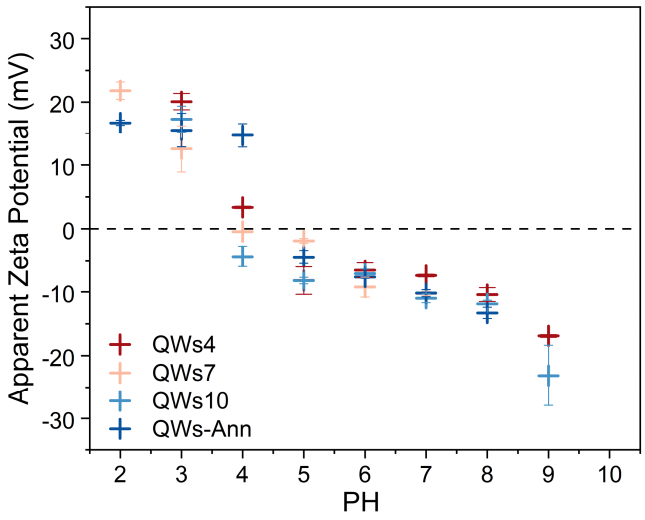

Figure R10. Zeta potential analysis and determination of the Point of Zero Charge (PZC) for SnO_2 QWs. The PZC values were determined through zeta potential measurements conducted in standard pH buffer solutions. The PZC is defined as the specific pH at which the net surface charge at the hydrodynamic shear plane approaches zero. Error bars represent the standard deviation derived from triplicate measurements.

The following text has been updated in the manuscript:

(Page 4, Lines 67-69) "The existence of the two pathways was supported by a strong correlation between the catalyst point of zero charge (PZC) and WD activity, indicating that high-PZC oxides are generally preferred catalysts for WD near the AEL."

Comment 5

On page 8 of the manuscript, the authors state that "Together with the EPR results, we concluded that both i-O_v and b-O_v concentrations increase with longer synthesis durations" which appears to contradict the data in Supplementary Table 4, where the concentration of i-Ov decreases over reaction time.

Furthermore, the characterization and quantitative analysis presented here appear to constitute critical experimental evidence, yet the manuscript lacks sufficient interpretation, making it difficult for readers to understand how the surface oxygen species are quantified.

Reply:

We sincerely thank the reviewer for pointing out this potential inconsistency. This arises from the different physical quantities probed by EPR, XPS, and Raman spectroscopy, rather than from conflicting experimental data.

EPR and XPS measurements probe the overall density of vacancy-related surface species. The EPR spectra quantify paramagnetic superoxide species (O_2^-) adsorbed at oxygen vacancy sites, and the corresponding spin density increases monotonically from QWs4 (9.16×10^{12} spins g^{-1}) to QWs10 (1.46×10^{13} spins g^{-1}), before decreasing upon annealing (**Supplementary Table 1**).

Supplementary Table 1. Quantification of paramagnetic superoxide species (O_2^-) in SnO_2.

Sample	QWs4	QWs7	QWs10	QWs-Ann
spins/g	9.16×10^{12}	1.09×10^{13}	1.46×10^{13}	2.02×10^{12}

In contrast, Raman spectroscopy does not provide absolute vacancy concentrations but resolves the relative distribution of vacancy types. Deconvolution of the 500-700 cm^{-1} region separates contributions from in-plane oxygen vacancies (i-O_v) and bridging oxygen vacancies (b-O_v). The Raman analysis shows that the fraction of i-O_v decreases from approximately 66% (QWs4) to 45% (QWs10), while the fraction of b-O_v increases from about 34% to 55% (**Supplementary Table 4**). These data indicate a redistribution of vacancy types toward bridging configurations rather than a decrease in total vacancy density.

Supplementary Table 4. Deconvolution of the Raman bands from 500 to 700 cm^{-1} for SnO_2 QWs.

Sample	**i-O_v (%)**	**b-O_v (%)**
QWs4	66	34
QWs7	55	45
QWs10	45	55.

To avoid misleading readers, we have clarified in the revised manuscript and Supplementary Information how each structural parameter was quantified. This additional clarification is intended to ensure that readers can clearly understand the origin and physical meaning of each variables.

We have revised the corresponding sentences in the main text to explicitly distinguish between total O_v concentrations and fractions of different O_v structures:

(Page 8, lines 157-158) “Together with the EPR results, we concluded that b-O_vs are preferentially enriched with longer synthesis durations.”

(Page 46, lines 421-429 in the Supplementary Information) “The $-O_{br}H$/b-O_v fraction from Raman peak-area analysis under consistent fitting constraints. The transmembrane voltage (TMV) is measured using a membrane potential-sensing setup under identical operating conditions at a catalyst loading of 14 μg cm^{-2}. The particle diameter (D) is determined from TEM statistical analysis. The specific surface area (S) is measured by N_2 adsorption–desorption using the BET method. The electrical conductivity (σ) is obtained from bulk conductivity measurements. The density (ρ) corresponds to the intrinsic material density; The superoxide-related signal (O_2^-) is quantified from EPR spectra and represents vacancy-associated paramagnetic electron states.”

Comment 6

Regarding central conclusion that $-O_{br}H$ govern the kinetics of water dissociation on SnO_2, the argument relies heavily on molecular simulations and lacks direct experimental evidence, which weakens its persuasiveness.

Reply:

We thank the reviewer for this important comment. In the revised manuscript, we have strengthened the experimental foundation by expanding the dataset and restructuring the argument around experimentally measurable material variables and data-driven analysis. Molecular simulations are used only to provide an atomistic interpretation.

To establish a broader experimental basis, we expanded the dataset to include seven systems spanning both intra-material modulation (SnO_2 QWs series) and cross-material validation (TiO_2), including QDs, QWs12 (**Figure R11**), rutile TiO_2 (R-TiO_2), and H_2-annealed rutile TiO_2 (H-Ann-R-TiO_2) (**Figure R12**). These systems systematically vary hydroxyl-related motifs while enabling comparison across distinct structural regimes. The QDs sample serves as a low $-O_{br}H$ limit, where reduced $-O_{br}H$ coverage corresponds to a higher TMV, consistent with hindered WD kinetics. The QWs12 sample probes the overgrowth regime of SnO_2 quantum wires, which does not further enrich $-O_{br}H$ and enhance WD activity. The R-TiO_2/H-Ann-R-TiO_2 comparison tests whether hydroxyl-related motifs influence WD kinetics beyond the SnO_2 system. The corresponding catalyst variables and WD performance are summarized in **Table R3**.

Table R3. Comparison of physicochemical properties and electrochemical performance of all samples.

Sample	Type	TMV (V)	-$O_{br}H$/b-O_V (%)	O_v ($\times10^{12}$ spins g^{-1})	Surface area (m^2 g^{-1})	Conductivity (S m^{-1})	Diameter (nm)	Density (g cm^{-3})
QWs4	SnO_2	1.07	34	9.16	165	0.0023	1.9	6.95
QWs7	SnO_2	0.90	45	10.92	153	0.0027	2.2	6.95
QWs10	SnO_2	0.88	55	14.55	158	0.0026	3.1	6.95
QWs12	SnO_2	0.89	53	13.85	156	0.0027	4.2	6.95
QDs	SnO_2	1.79	9	5.64	193	0.0025	2.5	6.95
R-TiO_2	TiO_2	1.74	12	4.31	23	0.0005	30	4.23
H-Ann-R-TiO_2	TiO_2	1.82	2	0.11	21	0.0059	34	4.23

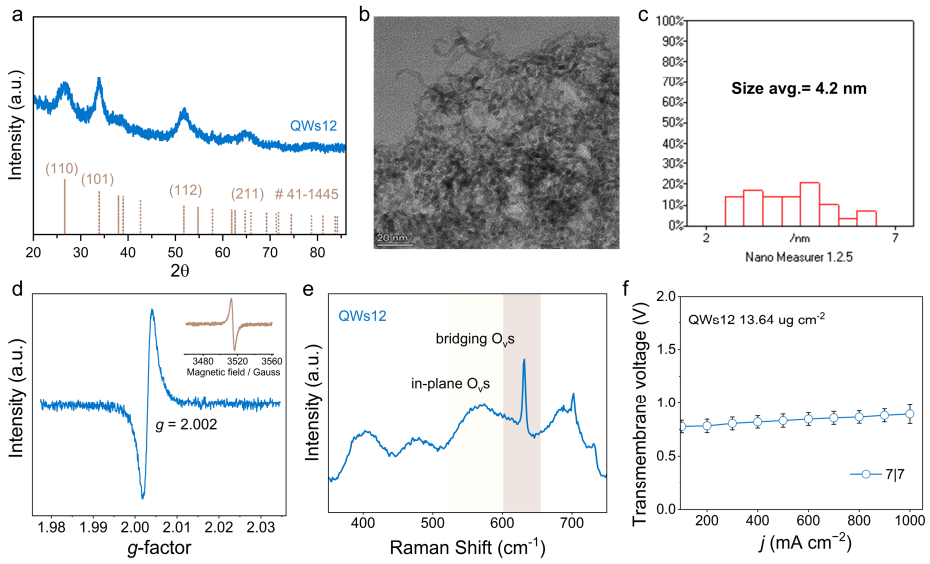

Figure R11. Characterization of SnO_2 QWs12. (a) PXRD patterns of QWs12. (b) High-resolution transmission electron microscopy (HRTEM) images and (c) corresponding particle size distribution histograms of QWs12. (d) EPR and (e) Raman spectra of QWs12. (f) TMV of QWs12 as the water dissociation (WD) catalyst at a loading of 14 μg cm^{-2} under pH 7|7 conditions.

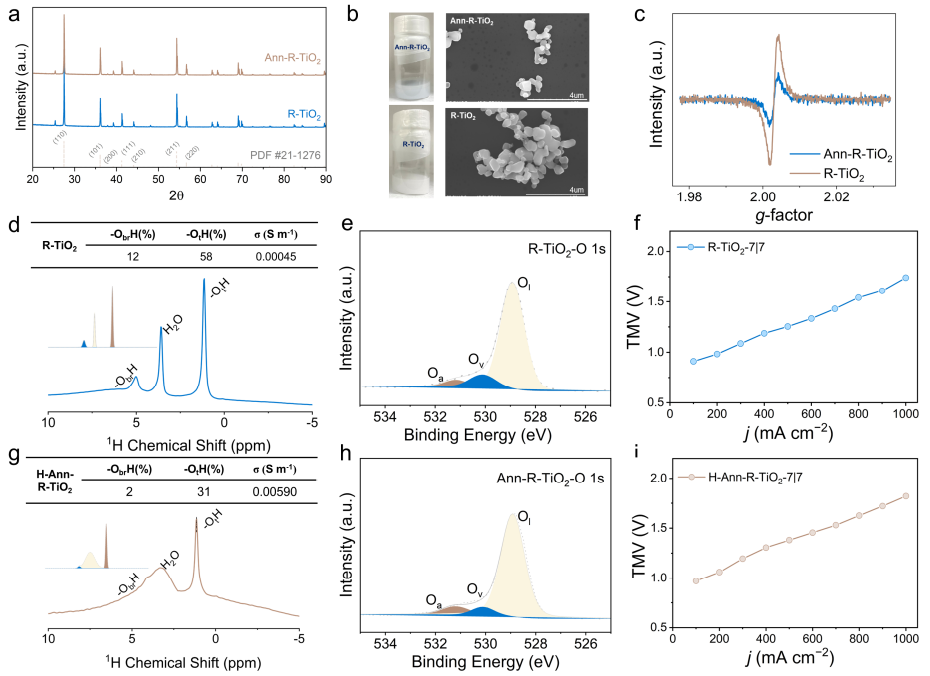

Figure R12. Characterization of R-TiO_2 and H-Ann-R-TiO_2. (a) PXRD patterns of pristine R-TiO_2 and hydrogen-treated H-Ann-R-TiO2. All diffraction peaks are indexed to the rutile phase (PDF #21-1276), indicating that hydrogen treatment does not alter the bulk crystal

structure. Inset: photographs of the corresponding catalyst inks. (b) Photographs and SEM images of R-TiO_2 and Ann- R-TiO_2. (c) Electron paramagnetic resonance (EPR) spectra indicating changes in paramagnetic defect species after H_2 treatment. Solid-state ^{1}H MAS NMR spectra and σ of (d) R-TiO_2 and (g) H-Ann-R-TiO_2. Resonances assigned to bridging hydroxyl, terminal hydroxyl, and adsorbed H_2O are indicated. O 1s XPS spectra of (e) R-TiO_2 and (h) H-Ann-R-TiO_2, deconvoluted into lattice oxygen (O_l), vacancy-associated oxygen (O_v), and surface hydroxyl/adsorbed oxygen species (O_a). TMV of BPM electrolyzers employing (f) R-TiO_2 and (i) H-Ann-R-TiO_2 as the water dissociation (WD) catalyst at a loading of 14 μg cm^{-2} under pH 7|7 conditions.

To briefly summarize the results, the role of $-O_{br}H$ is further supported by multiple independent experimental perturbations that systematically modulate hydroxyl-related motifs and yield consistent kinetic responses. First, within the SnO_2 QWs series (QWs4 to QWs10), controlled structural evolution leads to a monotonic increase in $-O_{br}H$ fraction, accompanied by a corresponding decrease in TMV **(Fig.2, Fig. 4a, Supplementary Figs. 14-15 and 32)**. Second, reverse validation through post-synthesis annealing independently confirms this trend. Suppression of vacancy-related and hydroxyl-associated features, as evidenced by XPS **(Supplementary Fig 7)** and EPR **(Supplementary Fig 26)** characterization, results in an increase in TMV **(Supplementary Fig. 16)**. Third, extending the synthesis duration to 12 h probes the overgrowth regime, in which further growth does not further enrich $-O_{br}H$ or enhance WD activity. (**Figure R11**). Fourth, pH-dependent measurements provide mechanistic consistency. The enhancement associated with higher $-O_{br}H$ fractions becomes more pronounced under alkaline-gradient conditions, where deprotonated surface species are expected to participate more actively in proton-transfer processes at the bipolar interface **(Fig. 2 and Supplementary Fig 31)**. Finally, cross-material validation using rutile TiO_2 further supports the generality of this relationship. H_2 treatment reduces surface hydroxyl density without altering bulk crystallinity, as confirmed by PXRD **(Figure R12a)** and solid-state ^{1}H MAS NMR **(Figures R12d, g)**. The H-Ann-R-TiO_2 sample exhibits inferior WD performance compared to pristine R-TiO_2 under both neutral and alkaline-gradient conditions **(Figures R12f, i)**.

Based on this expanded dataset, we performed Pearson correlation analysis across seven experimentally accessible catalyst variables, including TMV, $-O_{br}H$ fraction, O_v concentrations, particle size (D), conductivity (σ), surface area (S), and catalyst density (ρ) (**Figures R13, R14**). Among them, the $-O_{br}H$ fraction exhibits the strongest negative correlation with TMV ($r \approx -0.98$), whereas other variables show significantly weaker correlations. Hence, we concluded that the $-O_{br}H$ fraction is a measurable material variable that determines WD kinetics.

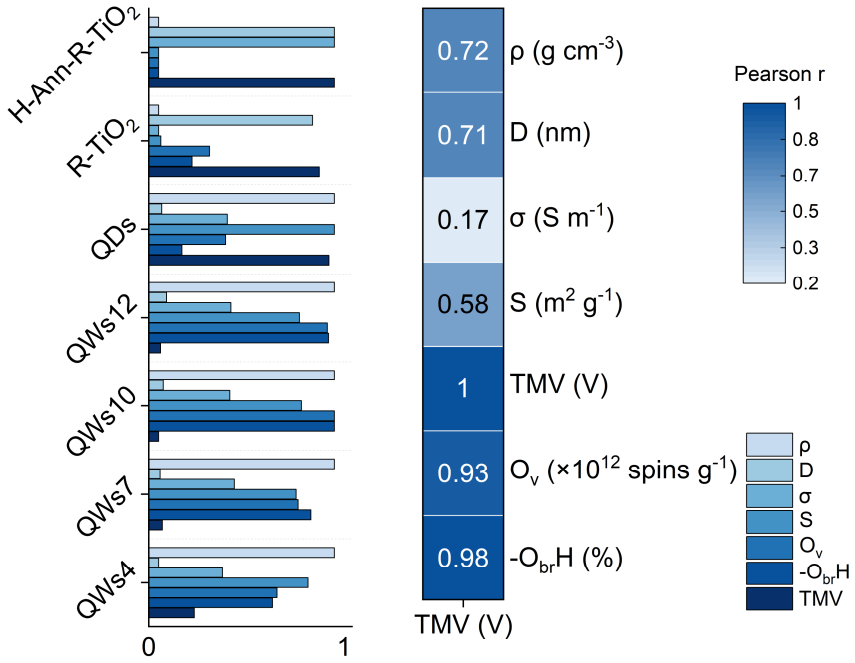

Figure R13. Normalized physicochemical variables and their correlation with water dissociation activity. All parameters are scaled using min–max normalization. The right panel summarizes the Pearson correlation coefficients (r) between TMV and each variable with color intensity indicating the magnitude of r.

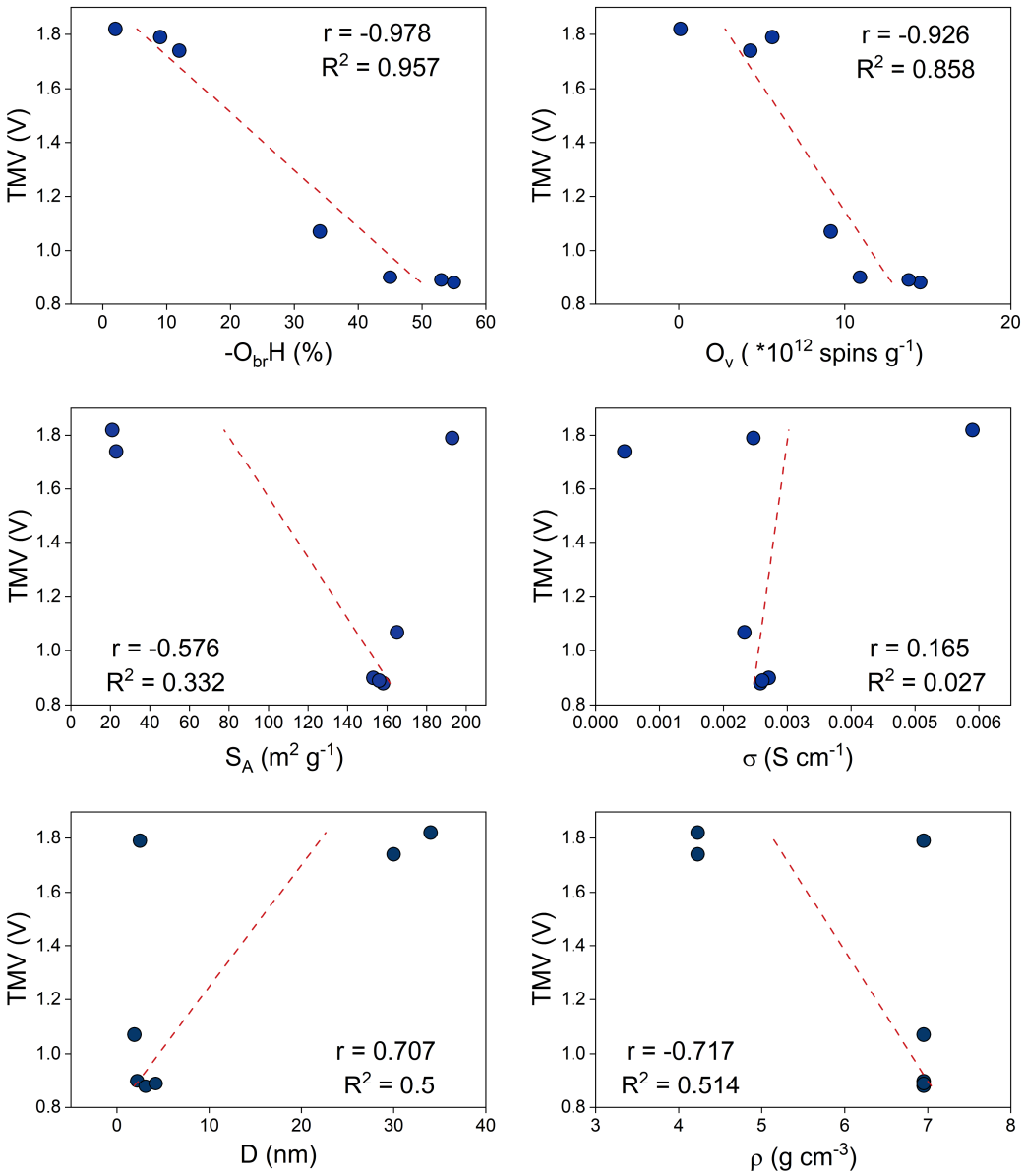

Figure R14. Scatter plots of TMV as a function of individual physicochemical variables.

Taken together, these experimental perturbations and statistical analyses provide a consistent and data-driven basis for the conclusion that −O_{br}H-associated motifs govern WD kinetics. Molecular simulations are not used as primary evidence; instead, they are employed only to rationalize how −O_{br}H-associated motifs may lower the kinetic barrier for proton transfer along the alkaline WD pathway.

We added **Figure R13** as **Figure 4c** and added the following sentence to the revised manuscript:

(Page 16, Lines 310-316) "To quantitatively resolve the structure–activity relationship, we performed Pearson correlation analysis across seven experimentally accessible catalyst variables, including TMV, −O_{br}H fraction, O_v concentrations, particle size (D), conductivity (σ), surface area (S), and catalyst density (ρ) (Fig. 4c, Supplementary Figs. 35, 36, and Supplementary Table 5). Among them, the −O_{br}H fraction exhibits the strongest negative

correlation with TMV (r ≈ -0.98), whereas other variables show significantly weaker correlations. Hence, we concluded that the $-O_{br}H$ fraction is a measurable material variable that determines WD kinetics."

(Page 15, Lines 293-296) "... (c) Normalized physicochemical variables and their correlation with water dissociation activity. All parameters are scaled using min–max normalization. The right panel summarizes the Pearson correlation coefficients (r) between TMV and each variable, with color intensity indicating the magnitude of r."

We added **Figures R11, R12,** and **R14** as **Supplementary Figures 33, 34, 36,** and **Table R3** as **Supplementary Table 5** to the revised supplementary information.

We have also added the following discussion to the revised manuscript:

(Page 16, line 302-308) " It should be noted that further prolonging synthesis duration to 12 h (i.e., QWs12 catalysts) yields comparable $-O_{br}H$ population and consequently WD activity (TMV ≈ 0.89 V) (Supplementary Fig. 33). We also confirmed the generality of the dependence of the WD activity on $-O_{br}H$ population using rutile TiO_2 (R-TiO_2) and H_2-annealed R-TiO_2 (H-Annealed-R-TiO_2) (Supplementary Fig. 34): H-Ann-R-TiO_2 exhibits an order-of-magnitude lower surface hydroxyl concentration (2 % vs. 12%) and markedly inferior WD activity (1.82 V vs. 1.74 V)."

(Page 19, line 378) " ... and QWs12 based on their reaction times of 4, 7, 10, and 12 hours, respectively."

Comment 7

For mechanistic studies of water dissociation catalysts in bipolar membranes, current densities should generally remain moderate (0–100 mA cm^{-2}), as higher current densities are limited by water supply to the bipolar membrane interior.

In this manuscript, however, the electrochemical characterization is performed at relatively high current densities (500 and 1000 mA cm^{-2}), which risks obscuring the genuine reaction and mass transport behavior in the water dissociation regime.

Reply:

We thank the reviewer for this important comment regarding the choice of current-density windows for the mechanistic analysis of water dissociation in BPMs. To clarify this point, we have added additional measurements and analysis spanning both moderate (0–50 mA cm^{-2}) and high (1000–2700 mA cm^{-2}) current-density regions.

First, we measured the transmembrane voltage (TMV) over a moderate current density range of 0–50 mA cm^{-2} (**Figure R15**).

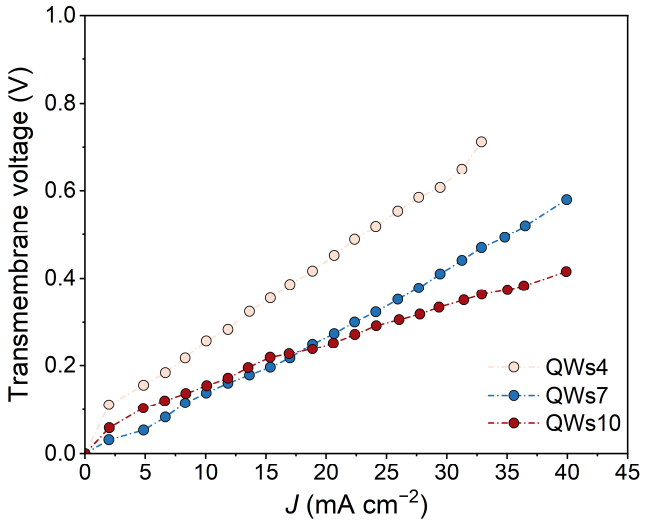

Figure R15. I-V (0 ~ 50 mA cm^{-2}) of the QWs.

In this regime, the polarization curves are smooth and do not exhibit curvature associated with transport limitation. Importantly, the relative activity trend (QWs4 < QWs7 < QWs10) observed at higher current densities is consistent with the 0–50 mA cm^{-2} range. This demonstrates that the correlation between $-O_{br}H$ enrichment and TMV reduction is established under moderate current densities.

Second, to evaluate the onset of possible internal water-transport limitation, we extended the polarization measurements to multi-ampere current densities under pure-water feed conditions **(Figure R16)**.

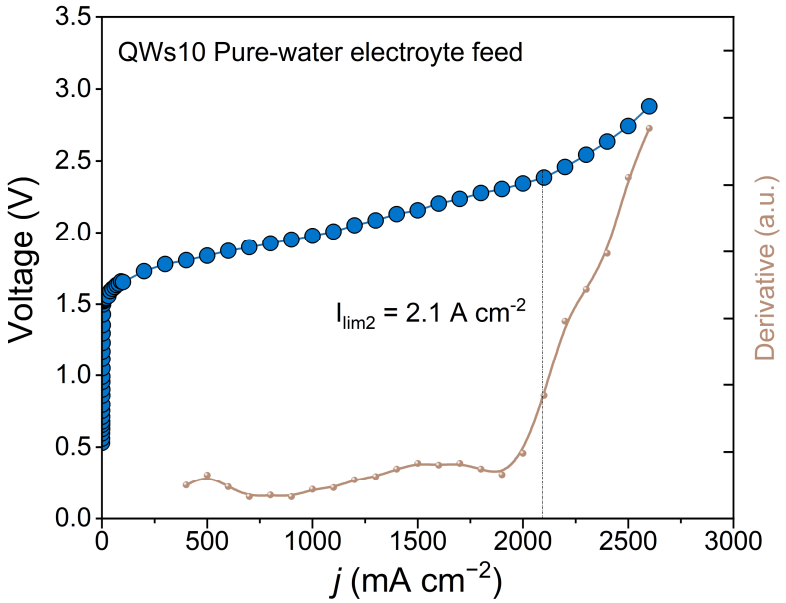

Figure R16. Polarization measurements of QWs10 up to 2.7 A cm^{-2}.

The polarization curve remains smooth and approximately linear between 1000 and 2000 mA cm^{-2}, and the differential resistance (dV/dj) does not show an abrupt increase in this region. A

pronounced upward curvature appears only beyond approximately 2.2 A cm^{-2}, which we identify as the second limiting current density (j_{lim2}). This behavior indicates that water-transport limitation occurs at substantially higher current densities than those used for catalyst comparison. Therefore, the current densities used for catalyst comparison in this work (≤ 1.0 A cm^{-2}) are below the identified transport-limited regime.

Taken together, these observations support that the mechanistic trends discussed in the manuscript are not dominated by water-supply limitation..

Reviewer #2

This manuscript offers an insightful look into how the enrichment of bridging hydroxyl species ($-O_{br}H$) boosts the alkaline water dissociation (WD) process on SnO_2 quantum wires. By combining thoughtful theoretical analysis with solid experimental evidence, it clearly shows that this enhancement is due to specific surface chemistry rather than to surface area alone. Overall, the study is interesting and relevant, providing both fundamental insights and practical performance data. Addressing the points above would enhance clarity and help computationally oriented readers follow the mechanistic conclusions more easily.

Reply:

We sincerely thank the reviewer for the comments and suggestions. We provide a detailed response to the questions below; we hope these answers address the reviewer's concerns.

Comment 1

The SnO_2(110) surface is a classic example of a rutile-type oxide, widely used in computational research. It would be helpful if the authors could include a brief explanation or cite relevant sources for their choice of a Sn-exposed surface rather than an O-terminated one, especially in the context of water dissociation. This discussion would clarify why this termination is particularly useful for highlighting the active bridging hydroxyl sites ($-O_{br}H$) and the associated alkaline WD process.

Reply:

To clarify the surface termination under specific conditions, the surface Pourbaix diagram was plotted for three common terminations (−O, −OH, and bare). As shown in **Figure R17**, three distinct surface states are accessible under aqueous conditions: the bare Sn-exposed surface, the hydroxylated surface ($-O_{br}H$-covered), and the fully oxidized surface (O*-covered). Importantly, under the investigated pH ranges relevant to water dissociation on SnO_2, the bare Sn-exposed surface is identified as the thermodynamically stable termination, justifying our choice of this surface model for subsequent free-energy calculations.

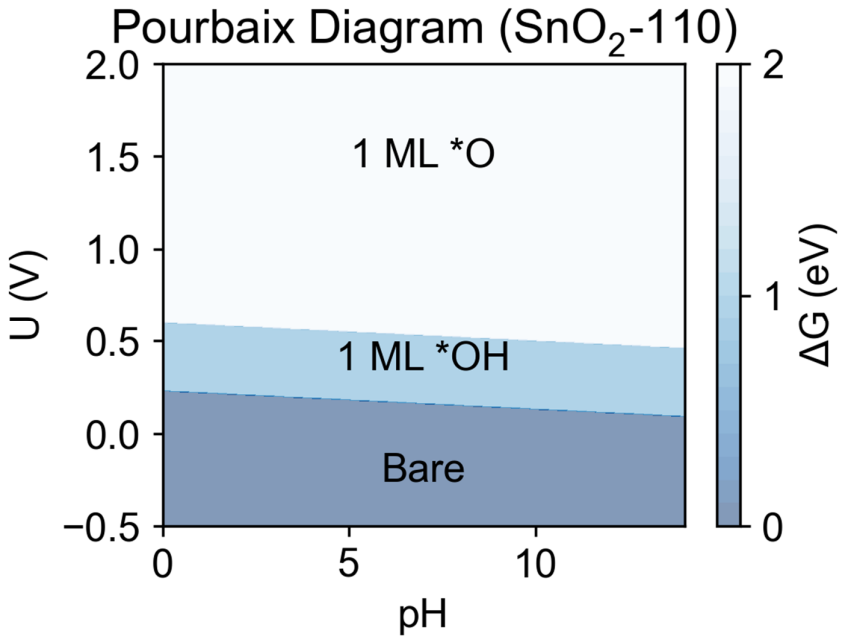

Figure R17. Surface Pourbaix diagram of SnO_2(110) with different terminations.

We added **Figure R17** as **Supplementary Figure 18** to the revised supplementary information.

We added the following sentence to the manuscript:

(Page 11, Lines 222-224) " The surface Pourbaix diagram suggests that under water dissociation conditions, SnO_2(110) is the most stable termination (Supplementary Fig. 18)."

Comment 2

The site's pKa is described via the two-state free energy difference. In Figure 3b, the reference state is (0, 0), and the second state is (1.0, 12). A local minimum exists between these points. Could the authors clarify why this intermediate was not used as the final state? A similar issue applies to Figure 3c.

Reply:

We thank the reviewer for this insightful observation. We would like to clarify the rationale for our choice of reference and final states in the two-state free-energy framework for pKa determination.

The pKa of a surface site is defined by the free-energy difference between the protonated and deprotonated states. In this framework, the two physically meaningful states are the fully protonated surface site (reference state) and the fully deprotonated surface site (final state).

We acknowledge the presence of a local minimum in the free-energy profile between the two endpoint states. Such a phenomenon is also exhibited in the recent paper (*Nat. Commun.,* 15, 10270 (2024)). However, this intermediate was not chosen as the final state for the following reasons:

1. Physical interpretation

The released proton is sufficiently distant from both the upper and lower interfaces, preventing interfacial effects on it. The local minimum represents a metastable intermediate configuration, such as a partially restructured surface or a transiently stabilized hydrogen-bonding arrangement at the interface. Such intermediates do not correspond to a stable, experimentally observable protonation state of the surface site, and therefore do not constitute a physically meaningful endpoint for pKa determination.

2. Two-state model requirement

The pKa, by definition, describes the equilibrium between two well-defined protonation states (protonated and deprotonated). Using an intermediate metastable state as the endpoint would yield a free energy difference that does not correspond to any experimentally measurable acid-base equilibrium.

Comment 3

The PES is explored using the DPMD method. Given that machine-learned molecular dynamics performed poorly beyond the training data, it would be helpful if the authors could provide additional details on the composition of the training and test datasets. Could the author share more details about the training and test data?

Reply:

Thanks for the suggestion to provide a detailed description of the DPMD method, which will also help replicate it clearly.

"The DPMD model was obtained from ElectroFace, an artificial intelligence-accelerated ab initio molecular dynamics dataset for electrochemical interfaces, developed by Jun Cheng's group from Xiamen University. The training dataset was generated using the DP-GEN concurrent learning package, which adaptively samples configurations through iterative training, exploration, and DFT labeling stages. The final dataset comprises 6000 structures of the SnO_2(110)/water interface (669 atoms): 600 structures randomly extracted from a 100 ps AIMD trajectory (the initial dataset) and 5400 structures collected via concurrent learning. MD exploration was performed at 330K, 430K, and 530K to ensure sufficient coverage of phase space."

The above reply has been incorporated into the manuscript on Page 29, lines 598-606.

Comment 4

DFT calculations were performed using a planewave energy cutoff of 400 Ry with the PBE functional. Please verify that this cutoff is sufficient.

Reply:

Thanks for the suggestion. We have thoroughly investigated this issue and performed a convergence test on the SnO_2-water interface across a range of planewave cutoffs. In the figures below, we compare the energies computed with 400 Ry, 500 Ry, and 600 Ry cutoffs (y-axis). The energy increment is ignored at 0.1%. So the 400 Ry with the PBE functional is sufficient in the current simulation.

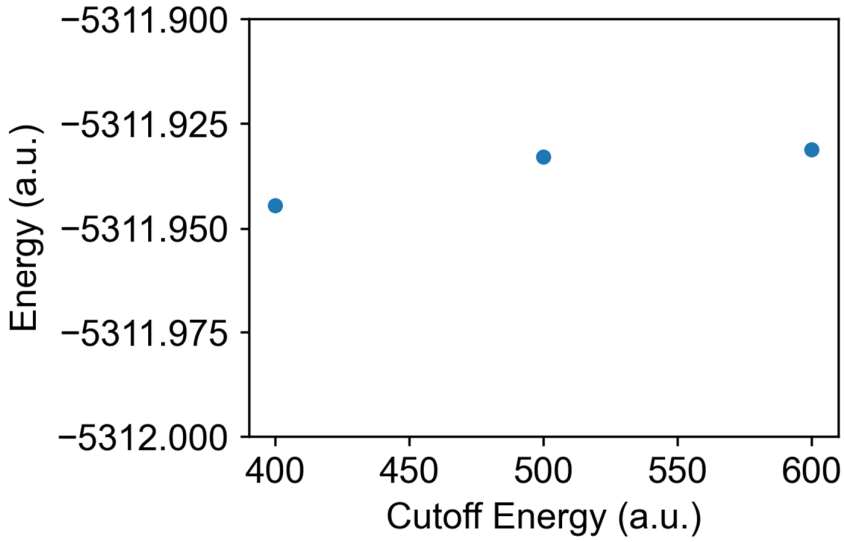

Figure R18. Convergence test of the planewave cutoff energy for the SnO_2–water interface.

Comment 5

The discussion primarily focuses on SnO_2-derived surfaces, raising questions about whether WD promotion is due to a general structure–activity principle linked to bridging hydroxyl motifs on rutile oxides or to a material-specific effect tied to the electronic properties of Sn–O bonding. Clarifying these aspects could strengthen the mechanistic argument and its broader relevance. To assess the transferability of the structure–activity relationship, oxide surfaces with similar bridging oxygen coordination environments could be studied under comparable conditions. Otherwise, the mechanism's consistency across different interfacial pH environments and membrane configurations.

Reply:

We thank the reviewer for this insightful comment on the universality of the proposed mechanism. To address this question, we extended our investigation to rutile TiO_2, which possesses a similar bridging oxygen coordination environment but a distinct metal–oxygen electronic structure. Pristine rutile TiO_2 (R-TiO_2) and hydrogen-treated rutile TiO_2 (Ann-R-TiO_2) were prepared and systematically characterized. XRD analysis confirms that both samples retain the rutile phase, with no secondary phases, indicating that the hydrogen treatment does not alter the bulk crystal structure (**Figure R19**). Solid-state ^{1}H MAS NMR spectroscopy was then employed to quantify surface hydroxyl populations. The spectra reveal that Ann-R-TiO_2 exhibits a reduced intensity of resonances assigned to bridging hydroxyl and terminal hydroxyl species compared to pristine R- TiO_2 under identical fitting and normalization conditions (*Nat. Mater.* **23**, 1421–1427 (2024)), indicating a lower surface hydroxyl content following treatment (**Figure R20**).

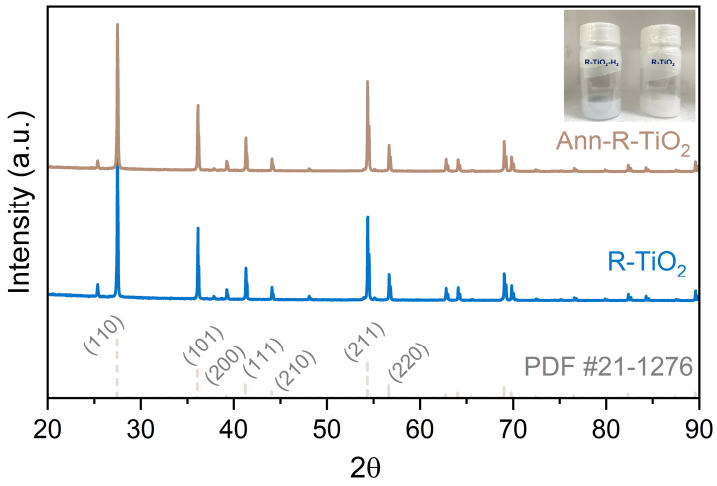

Figure R19. PXRD patterns of pristine R-TiO_2 and hydrogen-treated Ann-R-TiO_2. All diffraction peaks are indexed to the rutile phase (PDF #21-1276), indicating that hydrogen treatment does not alter the bulk crystal structure. Inset: photographs of the corresponding catalyst inks.

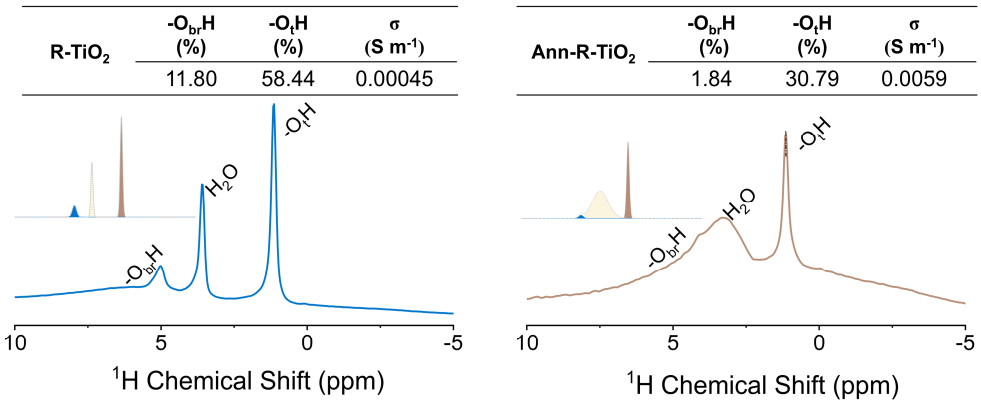

Figure R20. Solid-state ^{1}H MAS NMR spectra and σ of R-TiO_2 and Ann-R-TiO_2. Resonances assigned to bridging hydroxyl, terminal hydroxyl, and adsorbed H_2O are indicated.

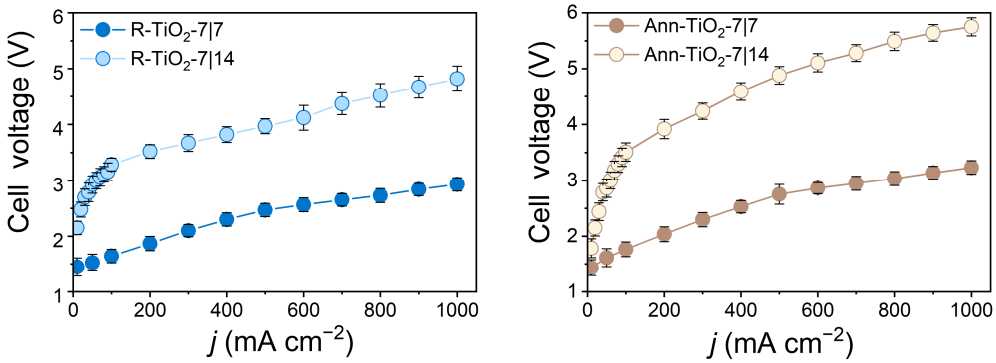

Figure R21. Full-cell polarization curves of BPM electrolyzers employing R-TiO_2 and Ann-R-TiO_2 as the water dissociation (WD) catalyst at a loading of 13.64 μg cm^{-2} under two distinct pH gradient conditions: (7|7) and (7|14).

We subsequently evaluated the WD performance of both TiO_2 samples in bipolar membrane (BPM) electrolyzers under identical catalyst loadings (14 μg cm^{-2}) and under two pH gradient conditions (7|7 and 7|14) (**Figure R21**). Under both electrolyte configurations, Ann-R-TiO_2 consistently exhibits higher cell voltages than pristine R-TiO_2 at the same current densities. Importantly, the performance difference is more pronounced under alkaline gradient conditions (7|14), consistent with the proposed role of bridging hydroxyl–associated sites in facilitating proton-transfer steps under deprotonated surface states. Because the bulk crystal phase and general rutile framework remain unchanged, the observed performance decline correlates directly with the reduction in surface hydroxyl content rather than with changes in bulk electronic structure.

These cross-material results demonstrate that modulation of bridging hydroxyl populations influences WD kinetics in rutile oxides beyond the specific case of SnO_2. The consistent trend between reduced $-O_{br}H$ abundance and diminished WD activity in both SnO_2 and TiO_2 systems supports a general structure–activity principle associated with bridging hydroxyl motifs on rutile-type oxide surfaces. While differences in intrinsic electronic properties between Sn–O and Ti–O frameworks may influence absolute activity levels, the directional dependence of WD performance on bridging hydroxyl abundance appears transferable across chemically distinct rutile oxides.

We added **Figures R19-R21** as **Supplementary Figure 35** to the revised supplementary information.

We added the following sentence to the manuscript:

(Page 16, Lines 304-308) "We also confirmed the generality of the dependence of the WD activity on $-O_{br}H$ population using rutile TiO_2 (R-TiO_2) and H_2-annealed R-TiO_2 (H-Annealed-R-TiO_2) (Supplementary Fig. 34): H-Ann-R-TiO_2 exhibits an order-of-magnitude lower surface hydroxyl concentration (2 % vs. 12%) and markedly inferior WD activity (1.82 V vs. 1.74 V)."

Comment 6

While the reported stability metrics are impressive, briefly clarify the structural or chemical persistence of $-O_{br}H$ under prolonged high-current operation. Including post-operation characterization (e.g., spectroscopic confirmation in the Supplementary Information) or discussing dynamic regeneration of $-O_{br}H$ sites during operation would strengthen the work.

Reply:

To clarify this point, we performed Raman spectroscopy on the QWs10 catalyst layer after continuous electrolysis at 1 A cm^{-2} for 10 h, and the results have been added to the Supplementary Information.

The post-electrolysis Raman spectrum shows that the characteristic bands assigned to in-plane oxygen vacancies (~571 cm^{-1}) and bridging oxygen vacancies (~629 cm^{-1}) remain clearly observable. Importantly, the bridging-vacancy-associated feature remains pronounced, indicating that $-O_{br}H$ motifs are retained during extended high-current electrolysis.

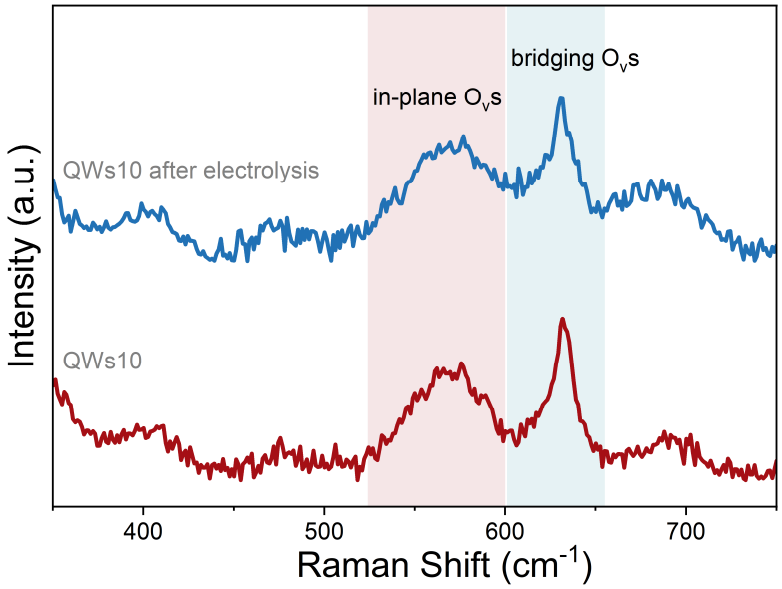

Figure R22. Raman spectrum of SnO_2 QWs10 recorded after 10 h electrolysis at 1 A cm^{-2}. The vacancy-related bands at ~571 cm^{-1} and ~629 cm^{-1}, assigned to in-plane and bridging oxygen vacancies, remain observable after operation, indicating the persistence of $-O_{br}H$-associated motifs.

We added **Figure R22** as **Supplementary Figure 41** to the revised Supplementary Information.

We have also added the following discussion to the revised manuscript:

(Page 18, line 349-351) "Post-operation Raman spectroscopy confirms the persistence of signatures associated with $-O_{br}H$ motifs after electrolysis (Supplementary Fig. 41)."

Reviewer #3:

The authors present a mechanism-oriented materials study that combines theory-driven design with experimental validation to elucidate structure–reactivity relationships in water dissociation within bipolar membranes. The work reveals the role of surface hydroxyl coordination in determining the reaction pathway and kinetics of water dissociation. This is imperative for understanding this fundamental process and developing more efficient catalysts and bipolar membranes. Overall, the study is timely and important. Several aspects of the manuscript require improvement. Issues in interpreting observed correlations, in data presentation, in performance comparisons with competing electrolyzer configurations, and in degradation mechanisms must be addressed. I therefore recommend major revision, with the expectation that a carefully revised manuscript addressing the points raised below would be suitable for publication.

Reply:

We would like to thank the reviewer for the positive comments and the very constructive suggestions, which will help us further improve the quality of our manuscript.

Comment 1

Line 107: The statement "These O_vs would transform into surface hydroxyls via water adsorption and dissociation" lacks sufficient supporting evidence. The authors are encouraged to validate this claim with either experimental or computational evidence.

Reply:

We thank the reviewer for raising this important point. To substantiate the claim that oxygen vacancies (O_vs) transform into surface hydroxyls via water adsorption and dissociation, we have performed additional machine-learning molecular dynamics (MLMD) simulations to provide direct atomistic evidence for this proposed mechanism.

Two initial structures were constructed based on the previously established slab model by selectively removing two distinct surface oxygen sites: the bridge oxygen site (O_{br}) and the planar oxygen site (O_{pla}), as illustrated in **Figure R23**. MLMD simulations were subsequently performed for approximately 150 ps to capture the full dynamical evolution of the vacancy healing process under aqueous conditions.

The simulations reveal two related pathways depending on the vacancy site:

1. Pathway A — Bridge site vacancy (O_{br}):

The oxygen vacancy at the bridge site is directly replenished by a neighboring oxygen atom from interfacial water molecules. The adsorbed water molecule undergoes spontaneous dissociation at the vacancy site, leaving one proton at the surface and forming a surface hydroxyl (–OH) group.

2. Pathway B — Planer site vacancy (O_{pla}):

The mechanism for the planar oxygen vacancy proceeds via a two-step relay process. In the first step, the planar vacancy is filled by a neighboring bridge oxygen atom through a local lattice rearrangement, effectively converting the planar vacancy into a bridge vacancy. In the

second step, the newly formed bridge vacancy follows the same healing trajectory as described in Pathway 1, being replenished by interfacial water oxygen and subsequently dissociating to form a surface hydroxyl.

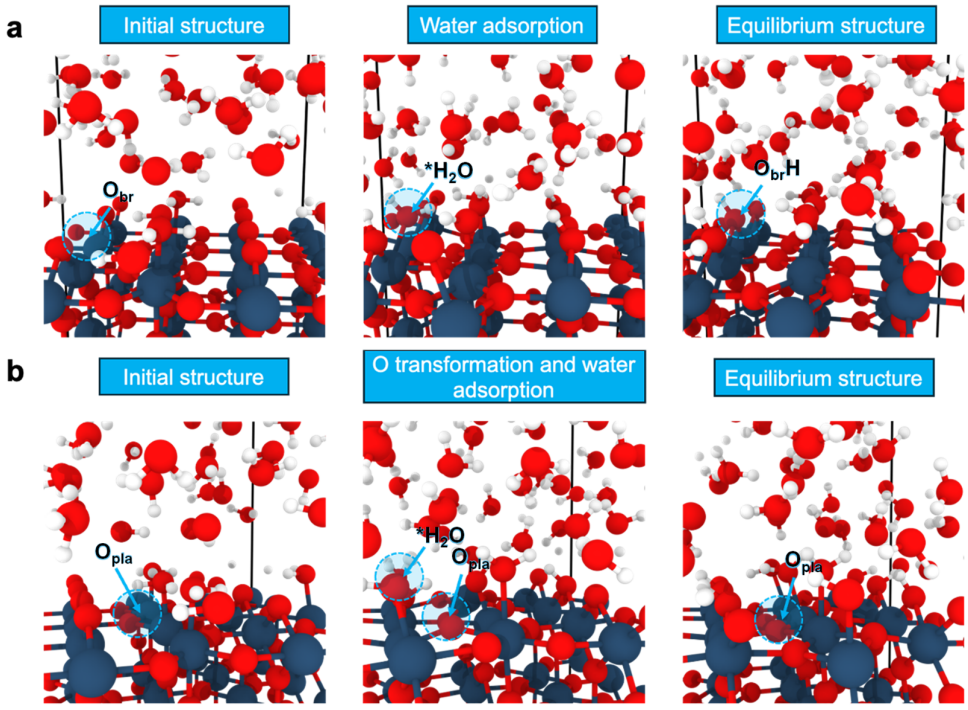

Figure R23. Schematic of the surface vacancy from the bridge and the planar site transformation during molecular dynamics simulations. (a) Pathway A: Direct healing of a bridge oxygen vacancy (O_v). MLMD snapshots illustrate that a vacancy at the bridge site is directly replenished by an oxygen atom from a coordinated interfacial water molecule. This process is followed by spontaneous water dissociation, resulting in the formation of a stable surface hydroxyl (-OH) group and the release of a proton. (b) Pathway B: Relay healing of a planar oxygen vacancy (O_{pla}). The transformation proceeds via a two-step mechanism: the planar vacancy is initially filled by a neighboring bridge oxygen atom through local lattice rearrangement, effectively migrating the vacancy to a bridge site; the newly generated bridge vacancy then undergoes the same water-mediated healing and dissociation process described in Pathway A. These simulations provide direct computational evidence that both types of surface vacancies serve as precursors for the formation of active surface hydroxyl motifs.

We added **Figure R23** as **Supplementary Figure 4** to the revised supplementary information.

We have also added the following discussion to the revised manuscript:

(Page 7, line 128-131) "These O_vs would transform into surface hydroxyls via water adsorption and dissociation, as further supported by additional machine-learning molecular dynamics (MLMD) simulations showing vacancy healing at both bridge and planar oxygen sites via water-assisted hydroxylation (Supplementary Fig. 4)."

Comment 2

What would happen if the synthesis duration of SnO_2 QWs is extended beyond 10 h? Will the ratios between different hydroxyls change, and will the observed correlation stay monotonic?

Reply:

We thank the reviewer for this insightful question regarding the structural and surface-chemical evolution beyond the 10 h synthesis condition. To address this point, we extended the reaction time to 12 h (denoted as QWs12) and performed systematic structural, defect, and electrochemical characterization under identical preparation and testing conditions. XRD analysis confirms that QWs12 remains in the rutile phase, with no detectable secondary phases (**Figure R24**), indicating that prolonging the synthesis does not induce a structural transformation. However, TEM measurements reveal continued crystal growth, with the average diameter slightly increasing from 3.1 nm for QWs10 to 4.2 nm for QWs12 (**Figure R25**). EPR measurements indicate a small reduction in spin density, from 1.46×10^{13} spins g^{-1} (QWs10) to 1.4×10^{13} spins g^{-1} (QWs12) (**Figure R26**). Raman analysis shows that the fractions of bridging-vacancy-associated motifs ($-O_{br}H$/b-O_v) are comparable between QWs10 and QWs12 (55% vs. 53%) (**Figure R27**).

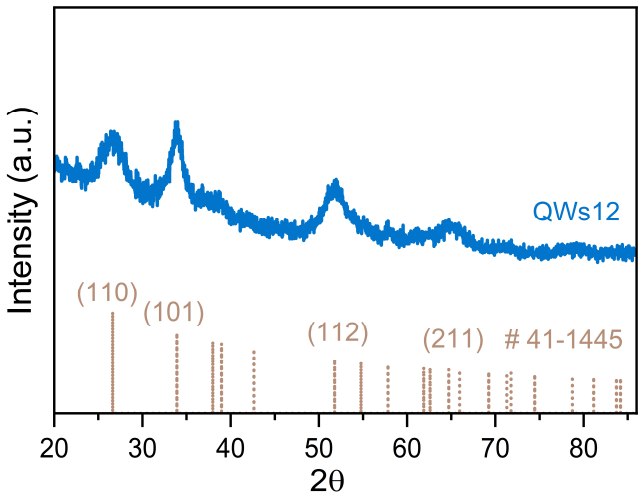

Figure R24. XRD spectra of QWs12.

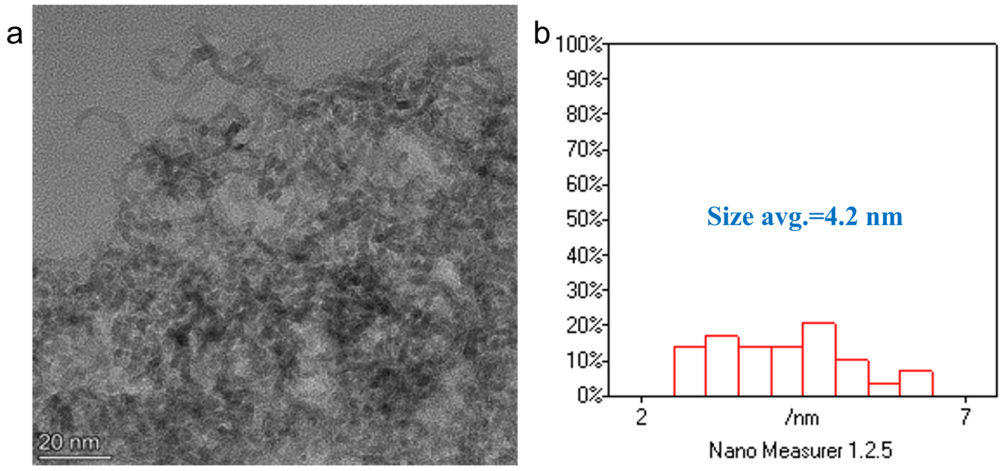

Figure R25. High-resolution transmission electron microscopy (HRTEM) images (a) and corresponding particle size distribution histograms (b) of QWs12.

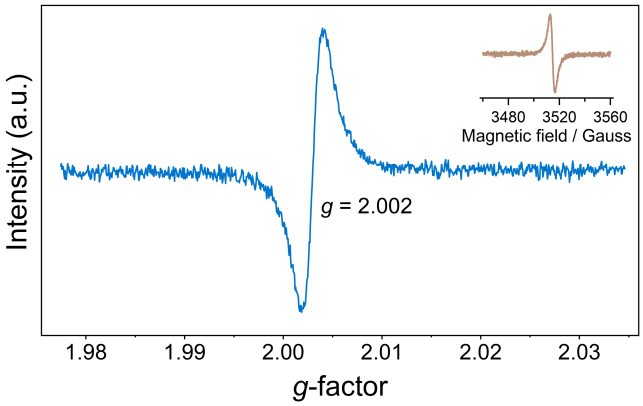

Figure R26. EPR spectra of QWs12.

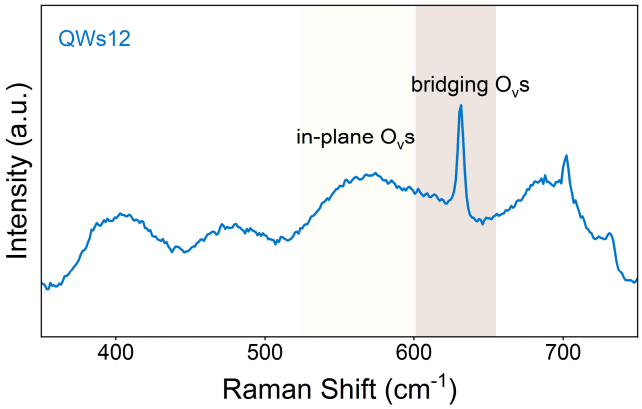

Figure R27. Raman spectra of QWs12.

In terms of the WD activity (**Figure R28**), the TMV follows the same trend. From QWs4 to QWs10, the $-O_{br}H$ fraction increases monotonically, and TMV decreases correspondingly (1.07 → 0.90 → 0.88 V). For QWs12, the comparable $-O_{br}H$ fraction of QWs12 to QWs10 offers nearly equivalent WD activity between the two catalysts (0.88 V vs. 0.89 V) at a mass loading of 14 μg cm^{-2} – extending the synthesis duration beyond 10 h does not further reduce the TMV.

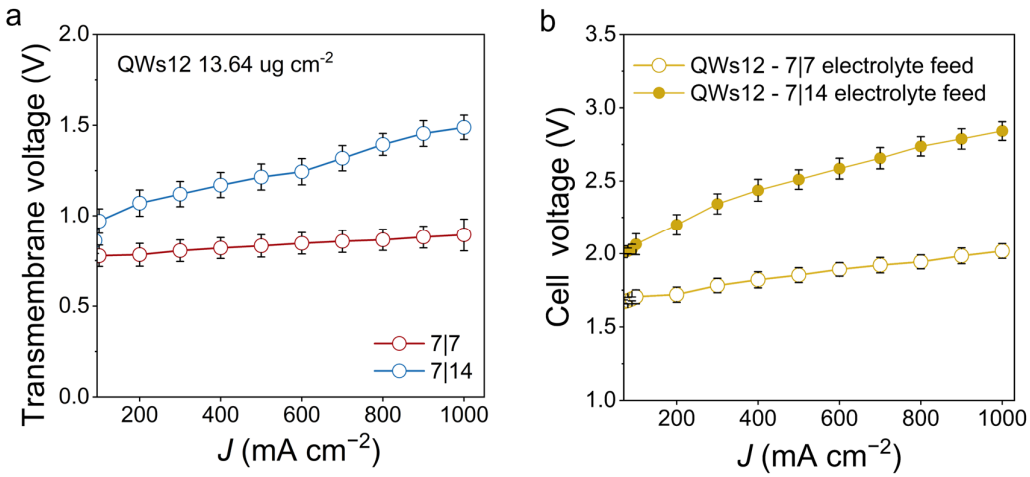

Figure R28. Transmembrane voltage (TMV) and cell voltage evaluated for QWs12 at a mass loading of 14 μg cm^{-2}.

Table R4. Physical properties, transmembrane voltage (TMV), and cell voltage of QWs12.

Sample	-O_{br}H/b-O_V (%)	TMV (V)	Cell voltage (V)	Surface area (m^2 g^{-1})	Conductivity (S m^{-1})	Diameters (nm)
QWs12	53	0.89	2.01	156	0.00261	4.2

We added **Figure R24-28** as **Supplementary Figure 34** to the revised supplementary information.

We have also added the following discussion to the revised manuscript:

(Page 16, lines 302-304) "It should be noted that further prolonging synthesis duration to 12 h (i.e., QWs12 catalysts) yields comparable $-O_{br}H$ population and consequently WD activity (TMV ≈ 0.89 V) (Supplementary Fig. 33)."

(Page 19, line 378) " ... and QWs12 based on their hydrothermal reaction times of 4, 7, 10, and 12 hours, respectively."

Comment 3

What are the meanings of the numbers in Fig. 4c, and how did the authors obtain them? Clarification and calculation details are apparently required to support the argument that "These results collectively demonstrate the link between TMV reduction and surface $-O_{br}H$ (Fig. 4c). In contrast, other reported activity descriptors, including surface areas, particle diameters, and electrical conductivity (Supplementary Table 5), show irrelevance to the observed WD activity improvement."

Reply:

We thank the reviewer for requesting clarification regarding the numerical values presented in Fig. 4c and the procedures used to obtain them.

The -$O_{br}H$ values shown in **Fig. 4c** are approximated by the fraction of bridging oxygen vacancies (b-Ov), which is used as a structural proxy for $-O_{br}H$-associated surface motifs. These values are derived from Raman spectral analysis in the 500–700 cm^{-1} region. Two characteristic bands at 571 cm^{-1} and 629 cm^{-1} are assigned to in-plane oxygen vacancies (i-Ov) and bridging oxygen vacancies (b-Ov), respectively. The spectra were fitted using two Lorentzian components after baseline subtraction, with identical fitting constraints applied to all samples. The integrated peak areas ($A_{i\text{-}Ov}$ and $A_{b\text{-}Ov}$) were extracted from the fitted curves, and the b-O_v fraction was calculated as:

$$b - Ov = \frac{A_{b-Ovs}}{A_{b-Ovs} + A_{i-Ovs}} \times 100\%$$

The resulting percentages (34%, 45%, and 55% for QWs4, QWs7, and QWs10, respectively) are reported in Supplementary Table 4.

The transmembrane voltage (TMV) is measured using a membrane potential-sensing setup under identical operating conditions at a catalyst loading of 14 μg cm^{-2}. The particle diameter (D) is determined from TEM statistical analysis. The specific surface area (S) is measured by N_2 adsorption–desorption using the BET method. The electrical conductivity (σ) is obtained from bulk conductivity measurements. The density (ρ) corresponds to the intrinsic material density; The O_v concentrations are quantified using superoxide-related signals (O_2^-) from EPR spectra that represent vacancy-associated paramagnetic electron states.

In addition, we clarify the presentation of Fig. 4c.

Based on this, we expanded the dataset (**Table R5**) and performed Pearson correlation analysis to replace the original pairwise linear fitting. The updated results are shown in **Figure R29**.

Table R5. Comparison of physicochemical properties and electrochemical performance of all samples.

Sample	Type	TMV (V)	-$O_{br}H$/b-O_V (%)	O_v ($\times 10^{12}$ spins g^{-1})	Surface area (m^2 g^{-1})	Conductivity (S m^{-1})	Diameter (nm)	Density (g cm^{-3})
QWs4	SnO_2	1.07	34	9.16	165	0.0023	1.9	6.95
QWs7	SnO_2	0.90	45	10.92	153	0.0027	2.2	6.95
QWs10	SnO_2	0.88	55	14.55	158	0.0026	3.1	6.95
QWs12	SnO_2	0.89	53	13.85	156	0.0027	4.2	6.95

QDs	SnO_2	1.79	9	5.64	193	0.0025	2.5	6.95
R-TiO_2	TiO_2	1.74	12	4.31	23	0.0005	30	4.23
H-Ann-R-TiO_2	TiO_2	1.82	2	0.11	21	0.0059	34	4.23

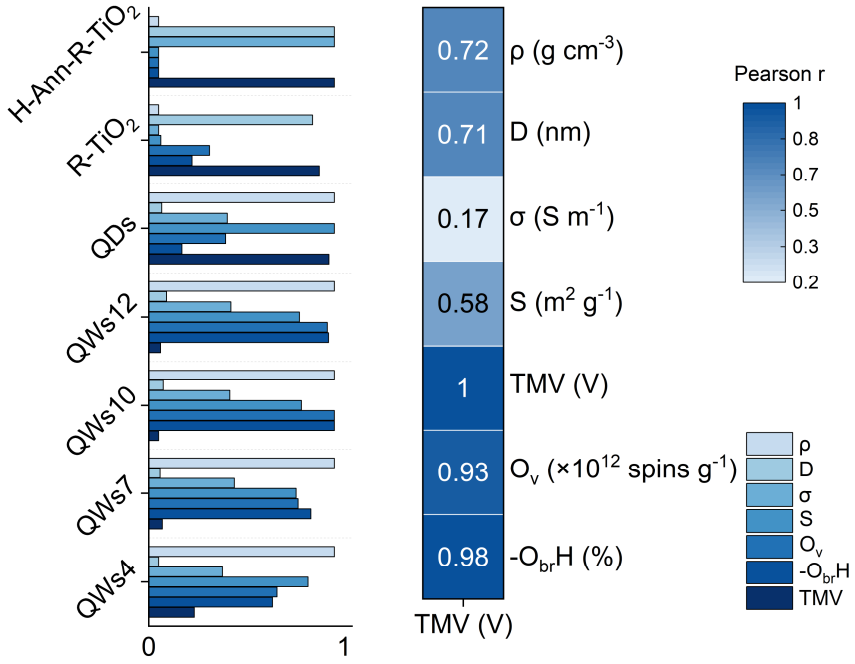

Figure R29. (c) Normalized physicochemical variables and their correlation with water dissociation activity. All parameters are scaled using min–max normalization. The right panel summarizes the Pearson correlation coefficients (r) between TMV and each variable, with color intensity indicating the magnitude of r.

We added **Figure R29** as **Figure 4c** to the revised manuscript.

We added **Table R5** as **Supplementary Table 5** to the revised supplementary information.

We have also added the following discussion to the revised manuscript:

(Page 15, lines 293-296) "(c) Normalized physicochemical variables and their correlation with water dissociation activity. All parameters are scaled using min–max normalization. The right panel summarizes the Pearson correlation coefficients (r) between TMV and each variable, with color intensity indicating the magnitude of r."

We have also added the following discussion to the revised supplementary information:

(Page 46, lines 421-429) "The $-O_{br}H$/b-O_v fraction from Raman peak-area analysis under consistent fitting constraints. The transmembrane voltage (TMV) is measured using a

membrane potential-sensing setup under identical operating conditions at a catalyst loading of 14 μg cm^{-2}. The particle diameter (D) is determined from TEM statistical analysis. The specific surface area (S) is measured by N_2 adsorption–desorption using the BET method. The electrical conductivity (σ) is obtained from bulk conductivity measurements. The density (ρ) corresponds to the intrinsic material density. The O_v concentration is quantified from EPR spectra using vacancy-associated paramagnetic electron states."

Comment 4

More broadly, while the use of acidic HER and alkaline OER in a reverse-bias BPM electrolyzer is mechanistically appealing, the voltage penalty associated with water dissociation at the BPM interface (reported as ~0.68 V at 100 mA cm^{-2}) appears substantial. From a system-level energy-efficiency perspective, this penalty may outweigh the kinetic benefits of avoiding alkaline HER and acidic OER. In contrast, anion exchange membrane water electrolysis (AEMWE) operates in a similar alkaline OER environment but incurs its primary kinetic penalty only at the HER, without an additional water-dissociation voltage loss.

The authors are therefore encouraged to compare the performance of their BPM water electrolyzer to that of state-of-the-art AEMWEs operated under comparable conditions. This helps clarify how much of the observed performance gap must be bridged for BPMs to become competitive, and under what scenarios—if any—the BPM approach offers a net advantage. Addressing this point would significantly strengthen the manuscript's relevance to the broader water electrolysis community.

Reply:

We thank the reviewer for raising this important system-level perspective.

From a thermodynamic standpoint, BPMWEs, PEMWEs, and AEMWEs share the same minimum cell voltage of 1.23 V. In BPMWEs, H^+ and OH^- are generated in situ at the bipolar junction via WD, and the associated Nernstian shifts of the half-reactions are compensated by the interfacial potential difference. Therefore, in the ideal limit of reversible proton-transfer kinetics and negligible junction resistance, BPMWEs do not incur an intrinsic thermodynamic penalty. The experimentally observed additional voltage thus reflects non-ideal interfacial kinetics and transport limitations.

To directly address the reviewer's concern, we compare our BPMWE performance with state-of-the-art AEMWE systems, as shown in **Figure R30**. In our system, the BPMWE employing the optimized QWs10 catalyst achieves a full-cell voltage of ~1.98 V at 1 A cm^{-2} under pure-water operation. In contrast, the AEMWE data reproduced from Hou *et al*. (*Science* 390, 294–298 (**2025**)) exhibit lower cell voltages over a comparable current density range. This comparison indicates that a performance gap still exists between current BPMWE systems and advanced AEMWEs.

Importantly, this gap can be largely attributed to the additional interfacial WD step in BPMWE. As demonstrated in this work, the WD-related voltage contribution is not fixed but can be systematically reduced through catalyst design. Specifically, increasing the density of −ObrH-associated motifs leads to a monotonic decrease in TMV across the QWs series, directly

demonstrating that the interfacial kinetic penalty is tunable. These results establish interfacial catalyst engineering as an effective pathway to mitigate the WD overpotential.

At the system level, BPMWE offers a distinct architectural advantage that is not accessible in AEMWE: spatial decoupling of acidic HER and alkaline OER within a single device. This enables operation under pure-water feed without the need for externally supplied concentrated electrolyte, while allowing each half-reaction to proceed under near-optimal pH conditions. In contrast, AEMWEs operate entirely under alkaline conditions, where HER kinetics and catalyst stability remain key constraints.

Taken together, while current BPMWE performance reflects a trade-off between WD kinetics and system efficiency, our results demonstrate a clear pathway toward closing this performance gap. By specifically targeting the dominant WD kinetic limitation through $-O_{br}H$ engineering, this work provides a mechanistically grounded strategy to reduce the interfacial voltage penalty and advance BPMWE toward practical competitiveness with state-of-the-art AEMWE systems.

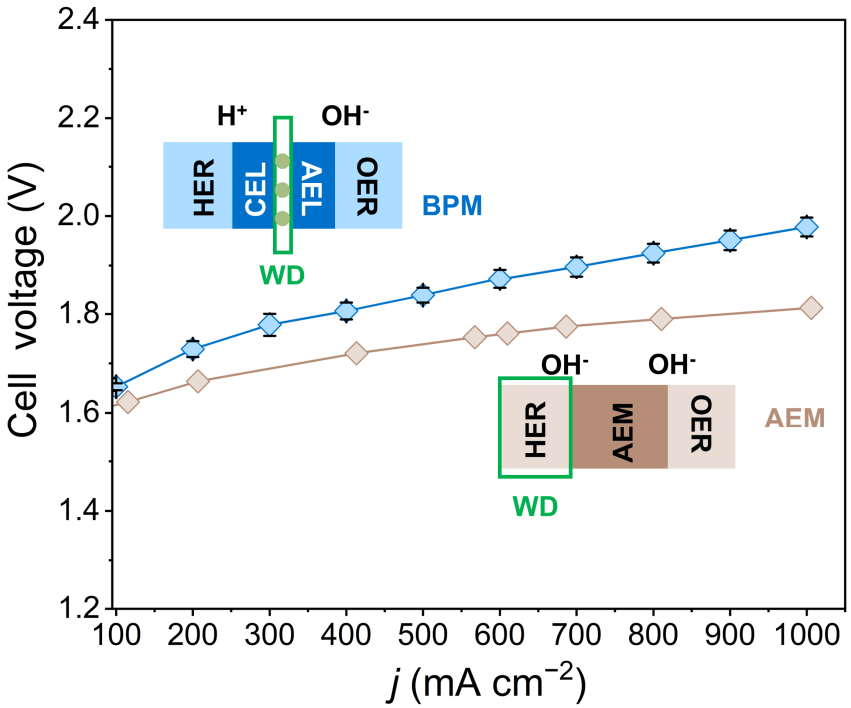

Figure R30. Performance comparison between BPM and AEM water electrolyzers. The AEM data are reproduced from Hou *et al.* (*Science* **390**,294-298(2025)). Schematic insets illustrate the distinct operating configurations: in the AEM electrolyzer, both electrodes operate under alkaline conditions, whereas in the BPM electrolyzer, hydrogen evolution (HER) occurs under locally acidic conditions and oxygen evolution (OER) under alkaline conditions, enabled by interfacial water dissociation (WD) at the bipolar junction. Error bars represent the standard deviation from independent measurements.

Comment 5

The attribution of activity degradation to Co_3O_4 dissolution (Line 299) remains speculative, as it relies solely on the qualitative observation of the anolyte turning yellowish. This causal link must be quantitatively substantiated. The authors should:
1) Quantify metal crossover: Utilize ICP-OES/MS to measure the concentration of dissolved Cobalt species in the anolyte at specific time intervals.
2) Post-mortem analysis on the spent Co_3O_4 electrode.

Reply:
We thank the reviewer for this important comment. To address this concern, we performed inductively coupled plasma optical emission spectroscopy (ICP-OES; Avio 200) measurements and post-mortem characterization of the Co_3O_4 anode.

Cobalt dissolution was quantified by analyzing electrolyte samples collected after different operation times. Prior to each measurement, the instrument was calibrated using a five-point standard curve (0, 0.5, 1.0, 2.0, and 5.0 μg L^{-1}) prepared from Co standard solutions in 1% HNO_3. All samples were appropriately diluted, and dilution factors were included in the final concentration calculations.

Under operating conditions at 1 A cm^{-2} in pure water electrolysis, the amount of dissolved cobalt is approximately 0.10 μg cm^{-2} after 24 h (**Figure R31**). The measured Co concentration increases further with extended operation time, reaching approximately 0.17 μg cm^{-2} after 36 h, indicating a gradual loss of cobalt during prolonged electrolysis.

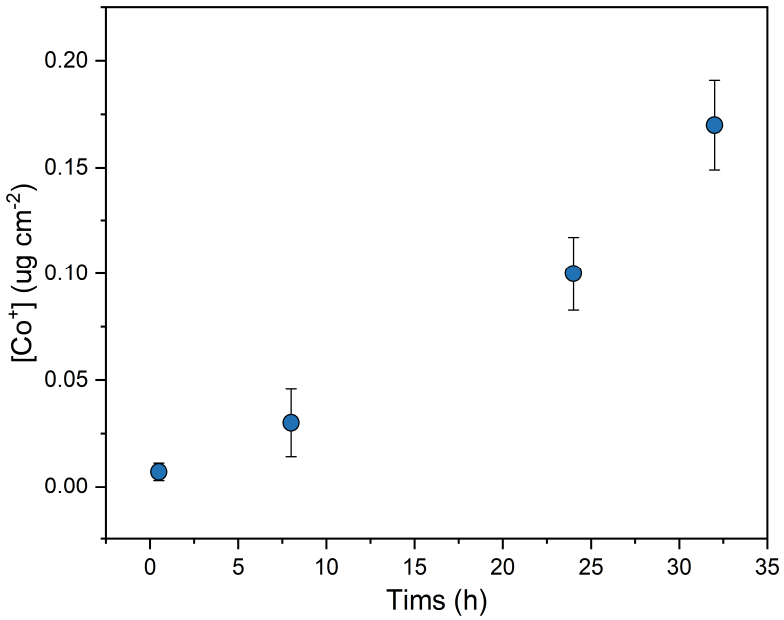

Figure R31. Dissolved Co quantified by ICP-OES from the electrolyte after electrochemical operation.

Post-mortem structural analysis of the Co_3O_4 anode was also performed. XRD patterns recorded after long-term operation show no detectable phase transformation, confirming preservation of the spinel structure (**Figure R32**). However, SEM–EDS elemental mapping reveals a measurable decrease in cobalt content relative to the pristine electrode, consistent with partial

material loss (**Figure R33**). Together, the quantitative ICP results and post-operation characterization support the conclusion that gradual Co dissolution contributes to the observed activity degradation.

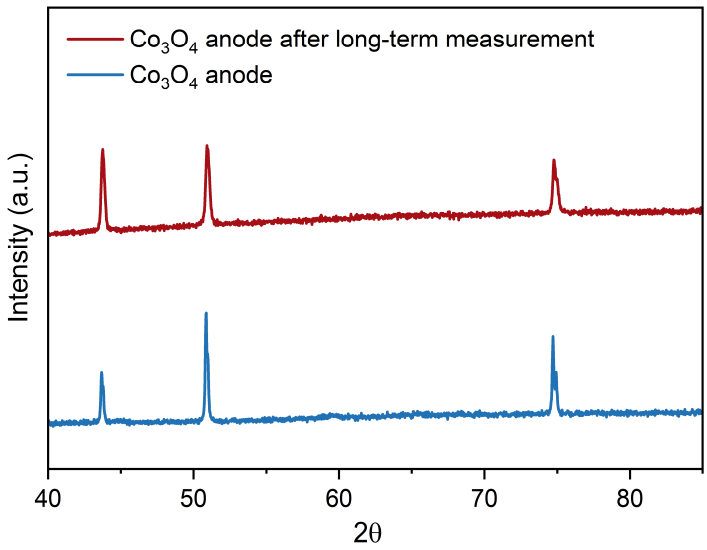

Figure R32. XRD patterns of the Co_3O_4 anode in the as-synthesized state and after electrochemical operation.

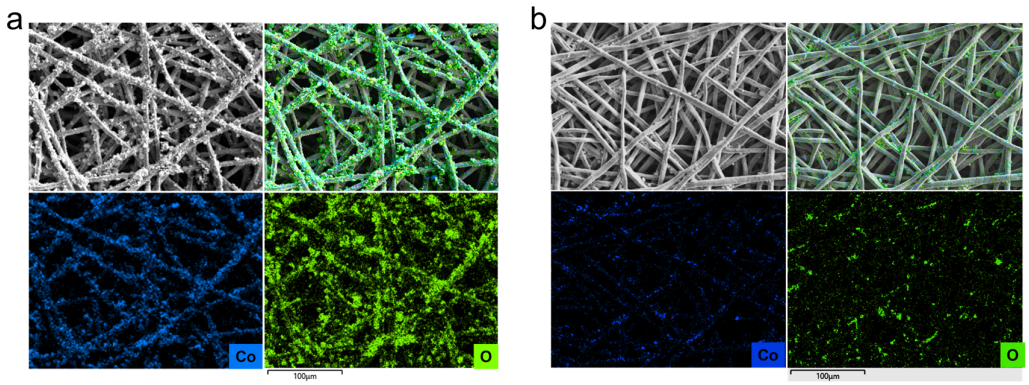

Figure R33. SEM images and corresponding EDS elemental mappings of the Co_3O_4 catalyst layer in the (a) as-synthesized state and (b) after long-term electrochemical operation.

We added **Figures R31-R33** as **Supplementary Figures 38-40** to the revised supplementary information.

We have also added the following discussion to the revised supplementary information:

(Page 43, lines 460-469) "Under operating conditions at 1 A cm^{-2} in pure water electrolysis, the amount of dissolved cobalt is approximately 0.10 μg cm^{-2} after 24 h. The measured Co concentration increases further with extended operation time, reaching approximately 0.17 μg cm^{-2} after 36 h, indicating a gradual loss of cobalt during prolonged electrolysis. XRD patterns recorded after long-term operation show no detectable phase transformation, confirming preservation of the spinel structure. However, SEM–EDS elemental mapping reveals a

measurable decrease in cobalt content relative to the pristine electrode, consistent with partial material loss. Together, the quantitative ICP results and post-operation characterization support the conclusion that gradual Co dissolution contributes to the observed activity degradation."

Comment 6

It might be helpful to check whether the density computed from the MLMD trajectory is reasonable.

Reply:

Thanks for your insightful suggestion. Following this recommendation, we evaluated the density obtained from the MLMD trajectories (**Figure R34**). The average density was computed from the equilibrated portion of the trajectory (after 50 ps), yielding ~1 g cm^{-3} in the bulk region, which is in good agreement with the expected density of liquid water under similar conditions.

This result confirms that the MLMD simulation provides a physically reasonable description of the system. The corresponding figure has now been added to the revised supporting information.

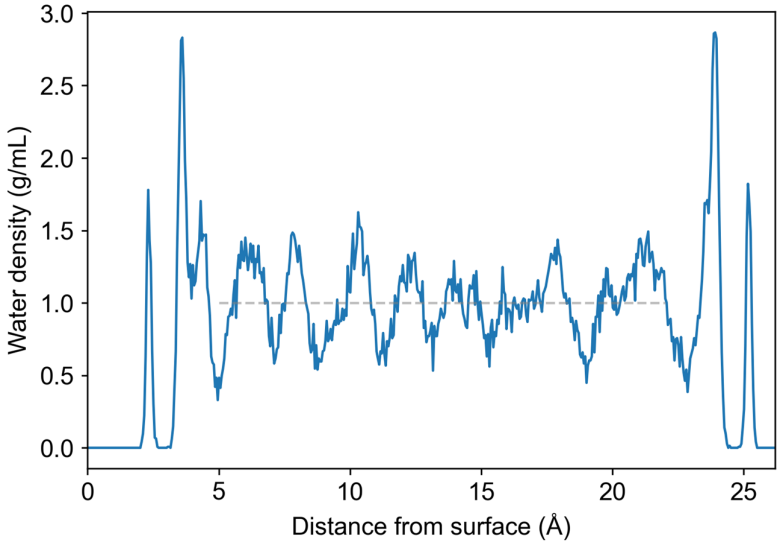

Figure R34. The water density distribution along the z-axis.

Comment 7

Fig. 4f appears intended to benchmark the performance of the present system against literature-reported state-of-the-art values. However, such comparisons are not straightforward, as reported performance metrics strongly depend on experimental conditions, including temperature, effective electrode area, electrolyte composition, and cell configuration. I recommend that the authors provide a more detailed summary of the experimental conditions associated with the literature data points, ideally in the Supplementary Information.

Reply:

We thank the reviewer for this important comment regarding the interpretation of the benchmarking data in Fig. 4f. We fully agree that performance comparisons among reported

bipolar membrane (BPM) and BPM-electrolyzer systems must be interpreted with caution, as the reported metrics depend strongly on experimental parameters such as electrolyte composition, operating temperature, active electrode area, and cell configuration.

To improve transparency and contextual clarity, we have revised and expanded the comparison table (**Table R6)**. The updated table provides, for each literature data point included in Fig. 4f, the corresponding current density and cell potential (with transmembrane potential where available), stability metrics and degradation rates, electrolyte composition, operating temperature, effective electrode area, cell configuration (e.g., MEA vs four-electrode setup), and full reference information.

Compared with the previous version, the revised table adopts a clearer structure that separates performance metrics from operating conditions and explicitly lists the electrolyte environment and cell architecture used in each study. This allows readers to directly assess differences in testing conditions across reports and to interpret Fig. 4f within the appropriate experimental context.

Table R6. Comparison of the performance of BPMs and BPM electrolyzers at high current densities.

Catalyst	Current density@Cell potential/Transmembrane potential	Stability @ current density and cell degradation rate	Electrolyte	Temperature	Electrode Area	Cell Configuration	Ref
SnO_2 QWs	**1 A cm^{-2} @ 1.98 V / 0.88±0.02 V**	**550 h @ 1 A cm^{-2} and 0.87 mV h^{-1}**	**H_2O**	**60 °C**	**1 cm^2**	**MEA**	**This Work**
	1 A cm^{-2} @ 1.89 V / N.A.	**450 h @ 0.5-1 A cm^{-2} and < 0.16 mV h^{-1}**	**0.5 M H_2SO_4 1 M KOH**	**60 °C**	**1 cm^2**	**MEA**	
3 nm SnO_2	1 A cm^{-2} @ 2.1 V / ~0.92 V *(a)*	100 h @ 1 A cm^{-2} and 2.4 mV h^{-1} *(b)*	H_2O	55 °C	1 cm^2	MEA	*Nat. Mater.* **23**, 1421–1427 (2024)
IrO_2|NiO	0.5 A cm^{-2} @ 2.2 V /1.10 V	4 h @ 0.5 A cm^{-2} and 10 mV h^{-1}	H_2O	50 °C	4 cm^2	MEA	*Science* **369**, 1099–1103 (2020)
GO-NCA	1 A cm^{-2} @ 2.7 V / 0.92 V	400 h @ 0.5 A cm^{-2} and 2 mV h^{-1}	H_2O	80 °C	4 cm^2	MEA	*Energy Environ. Sci.* **18**, 728–737 (2025)
	1 A cm^{-2} @ 1.9 V / N.A.	90 h @ 0.1 A cm^{-2} and N.A	0.5 M H_2SO_4 1 M KOH	80 °C	4 cm^2	MEA	
SnO_2	1 A cm^{-2} @ 2.68 V / 0.95 V	1000 h @ 0.3-0.5 A cm^{-2} and 1.1 mV h^{-1}	H_2O	60 °C	4 cm^2	MEA	*Nat. Commun.* **15**, 10220 (2024)
SnO_2@MBM	1 A cm^{-2} @ 2.3 V / 1.13 V	550 h @ 0.3 A cm^{-2} and 57.1 mV h^{-1}	0.5 M Na_2SO_4	RT	1 cm^2	Four-electrode cell	*Nat. Commun.* **14**, 1619 (2023)
CIBM	1 A cm^{-2} @ 3.95 V / 1.17 V	210 h @ 1 A cm^{-2} and 0.3 mV h^{-1}	1 M KOH with 2000 ppm KNO_3	RT	1 cm^2	Four-electrode setup	*Energy Environ Sci.* **16**, 3815–3824 (2023)

TiO_2	0.5 A cm^{-2} @ 2.6 V / N.A.	N.A.	N.A.	N.A.	N.A.	MEA	*Joule* **7**, 765–781 (2023)
TiO_2	0.5 A cm^{-2} @ 3.6 V / N.A.	20 h @ 0.25 A cm^{-2} and 23.3 mV h^{-1}	Seawater	50 °C	1 cm^2	MEA	*Joule* **7**, 765–781 (2023)
TiO_2-P25	0.5 A cm^{-2} @ 2.05 V / N.A.	N.A.		55 °C	1 cm^2	MEA	*Nat. Commun.* **13**, 3846 (2022)
IrO_X	0.5 A cm^{-2} @ 1.95 V / N.A.			55 °C	1 cm^2	MEA	

We added **Table R6** as **Supplementary Table 6** to the revised supplementary information.